Evaluating the Plausible Range of N$_2$O Biosignatures on Exo-Earths: An Integrated Biogeochemical, Photochemical, and Spectral Modeling Approach

Edward W. Schwieterman[1,2,3,4] , Stephanie L. Olson[2,5] , Daria Pidhorodetska[1,2,3] , Christopher T. Reinhard[2,3,6],
Ainsley Ganti[7], Thomas J. Fauchez[3,8,9,10] , Sandra T. Bastelberger[8,10,11,12] , Jaime S. Crouse[8,10,11,13] ,
Andy Ridgwell[1,2] , and Timothy W. Lyons[1,2,3]

[1] Department of Earth and Planetary Sciences, University of California, Riverside, CA, USA; eschwiet@ucr.edu
[2] NASA Alternative Earths Team, Riverside, CA, USA
[3] NASA NExSS Virtual Planetary Laboratory Team, Seattle, WA, USA
[4] Blue Marble Space Institute of Science, Seattle, WA, USA
[5] Department of Earth, Atmospheric, and Planetary Science, Purdue University, West Lafayette, IN, USA
[6] School of Earth and Atmospheric Sciences, Georgia Institute of Technology, Atlanta, GA, USA
[7] The Potomac School, 1301 Potomac School Rd, McLean, VA 22101, USA
[8] NASA Goddard Space Flight Center, 8800 Greenbelt Road, Greenbelt, MD 20771, USA
[9] American University, Washington, DC, USA
[10] Sellers Exoplanet Environment Collaboration (SEEC), NASA GSFC, USA
[11] Department of Astronomy, University of Maryland, College Park, MD 20742, USA
[12] Center for Research and Exploration in Space Science and Technology, NASA/GSFC, Greenbelt, MD 20771, USA
[13] Southeastern Universities Research Association (SURA), 1201 New York Avenue NW, Washington, DC 20005, USA

Abstract

Nitrous oxide (N$_2$O)—a product of microbial nitrogen metabolism—is a compelling exoplanet biosignature gas with distinctive spectral features in the near- and mid-infrared, and only minor abiotic sources on Earth. Previous investigations of N$_2$O as a biosignature have examined scenarios using Earthlike N$_2$O mixing ratios or surface fluxes, or those inferred from Earth's geologic record. However, biological fluxes of N$_2$O could be substantially higher, due to a lack of metal catalysts or if the last step of the denitrification metabolism that yields N$_2$ from N$_2$O had never evolved. Here, we use a global biogeochemical model coupled with photochemical and spectral models to systematically quantify the limits of plausible N$_2$O abundances and spectral detectability for Earth analogs orbiting main-sequence (FGKM) stars. We examine N$_2$O buildup over a range of oxygen conditions (1%–100% present atmospheric level) and N$_2$O fluxes (0.01–100 teramole per year; Tmol $= 10^{12}$ mole) that are compatible with Earth's history. We find that N$_2$O fluxes of 10 [100] Tmol yr^{-1} would lead to maximum N$_2$O abundances of ∼5 [50] ppm for Earth–Sun analogs, 90 [1600] ppm for Earths around late K dwarfs, and 30 [300] ppm for an Earthlike TRAPPIST-1e. We simulate emission and transmission spectra for intermediate and maximum N$_2$O concentrations that are relevant to current and future space-based telescopes. We calculate the detectability of N$_2$O spectral features for high-flux scenarios for TRAPPIST-1e with JWST. We review potential false positives, including chemodenitrification and abiotic production via stellar activity, and identify key spectral and contextual discriminants to confirm or refute the biogenicity of the observed N$_2$O.

Unified Astronomy Thesaurus concepts: Astrobiology (74); Exoplanet atmospheres (487); Exoplanets (498); Habitable planets (695); Nitrous oxide (1114); Biosignatures (2018)

1. Introduction

To date, over 5000 exoplanetary systems have been discovered (Christiansen 2022),[14] including several planets that are rocky in composition and located within the circumstellar habitable zone of their host star (Kane et al. 2016; Kaltenegger et al. 2019). The James Webb Space Telescope (JWST) will allow us to probe the atmospheres of a small number of these temperate terrestrial exoplanets, such as the TRAPPIST-1 planets (Gillon et al. 2017; Luger et al. 2017; Morley et al. 2017; Lincowski et al. 2018; Fauchez et al. 2019; Lustig-Yaeger et al. 2019; Ducrot et al. 2020), while upcoming ground-based extremely large telescopes will facilitate the

examination of nearby potentially habitable worlds, such as Proxima Centauri b (Anglada-Escudé et al. 2016; Ribas et al. 2016; Snellen et al. 2017; Meadows et al. 2018a). Ambitious future mission concepts, such as the IR/optical/UV observatory recommended by the 2020 Astronomy and Astrophysics Decadal Survey (National Academies of Sciences, Engineering, and Medicine 2021), or ESA's mid-IR (MIR) Large Interferometer for Exoplanets (LIFE) concept (Defrère et al. 2018; Quanz et al. 2018, 2022), would allow for the unprecedented atmospheric characterization of a larger number of temperate rocky planets orbiting stars in the solar neighborhood (most of which are yet to be discovered), though the observability of specific spectral features will be limited by the wavelength regime and observing mode.

One of the most compelling drivers of exoplanet science is the search for inhabited planets like Earth, which may be identified through remote spectroscopic biosignatures (Des Marais et al. 2002; Seager et al. 2012; Grenfell 2017; Kaltenegger 2017; Schwieterman et al. 2018). For such

---
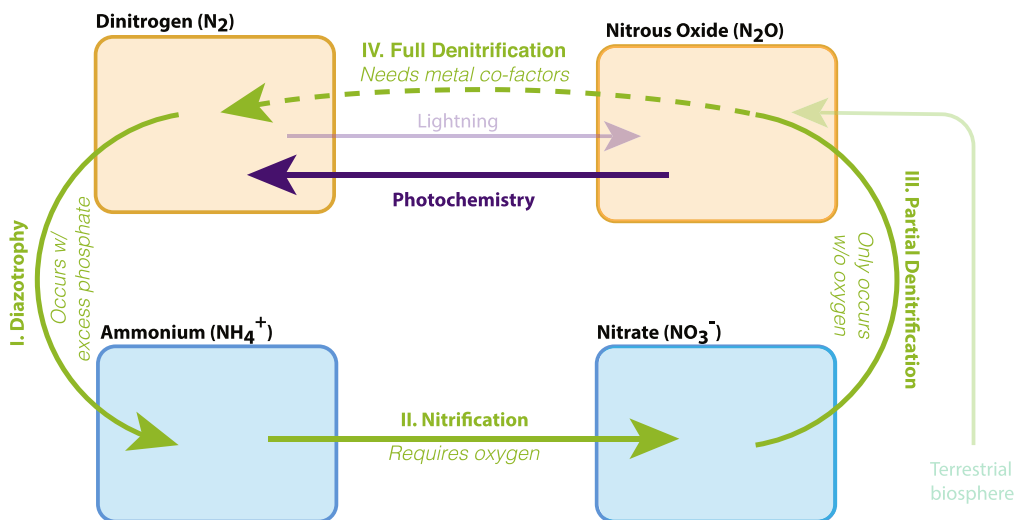
[14] https://exoplanets.nasa.gov/

Figure 1. A schematic nitrogen cycle as implemented in the biogeochemical model cGENIE. The faded and dashed lines signify processes that are not explicitly included in the scheme. N_2O fluxes result from incomplete denitrification of fixed nitrogen (NO_3^-) via the nitrous oxide reductase enzyme. Denitrification is an anaerobic process that depends on organic C fluxes, which are ultimately limited by nutrient (PO_4^{3-}) availability. A deficit of enzymatic catalysts—such as copper (Cu) —due to ocean water chemistry or initial planetary abundances would result in the partial termination of the N redox cycle and may produce large N_2O fluxes. In the extreme scenario of no enzymatic catalysts, or if the nitrous oxide reductase enzyme (or an analog) had not evolved, the N_2O flux would equal the total denitrification flux. Photochemical reactions will eventually return N_2O to N_2 in the atmosphere.

inhabited worlds to be positively identified from atmospheric spectra, they must possess global biospheres with a robust exchange of gases between life and the atmosphere as well as generate biosignature features that can be remotely detectable with foreseeable technologies and are separable from false-positive signals generated by abiotic processes (Catling et al. 2018; Meadows et al. 2018b; Schwieterman et al. 2018). Many groups have recently undertaken studies to assess the longevity and potential detectability of a variety of biosignature gases with near-future observational capabilities (Reinhard et al. 2017a; Fujii et al. 2018; Kawashima & Rugheimer 2019; Kaltenegger et al. 2020b; Pidhorodetska et al. 2020; Sousa-Silva et al. 2020; Checlair et al. 2021; Lin et al. 2021; Phillips et al. 2021; Wunderlich et al. 2021; Ranjan et al. 2022).

The coexistence of N_2 and O_2 in an atmosphere is one possible biosignature. This possibility is due to both the high chemical disequilibrium between N_2, O_2, and surface liquid water (Krissansen-Totton et al. 2016, 2018) and the planetary evolution that is required to accumulate large quantities of both gases, including the implausibility of the abiotic generation and atmospheric retention of these gases together given competing atmospheric and geochemical sinks (Stüeken et al. 2016; Lammer et al. 2019; Sproß et al. 2021). However, N_2 is itself challenging to detect directly, due its status as a homonuclear molecule with no transitional dipole moment, possessing weak collisional-induced absorption bands at 4.3 and 2.15 μm (Lafferty et al. 1996; Schwieterman et al. 2015).

In addition to N_2 gas (in the atmosphere and dissolved in the ocean), nitrogen on the present-day Earth exists in a wide variety of different chemical forms, ranging from reduced NH_4^+ to oxidized NO_3^-, with many intermediate redox species in between, including N_2O. Overall, Earth's nitrogen cycle can be thought of as the biologically driven removal of N_2 from the ocean and atmosphere, the fixation of nitrogen in organic matter, which is then followed by the recycling of nitrogen back to the atmosphere as N_2 (Figure 1; Thamdrup 2012; Tian et al. 2015). However, as a reflection of the diversity of microbial metabolisms, the recycling loop contains multiple

pathways back to N_2. One of these recycling routes involves the creation N_2O, which can either be further reduced biologically to N_2 or escape directly across the air–sea interface into the atmosphere.

Denitrification (the transformation of NO_3^- to N_2 gas, with N_2O as an intermediate product) is a relatively ubiquitous metabolism on Earth, and consequent N_2O production can be mediated both by bacteria as well as by some fungi (Chen et al. 2015). Additionally, the direct oxidation of ammonia by bacteria and archaea can also produce N_2O (Santoro et al. 2011; Prosser & Nicol 2012). Biological fluxes of N_2O into the atmosphere are several orders of magnitude larger than abiotic sources, such as lightning, which is estimated to produce $\sim$0.002% of atmospheric N_2O (Schumann & Huntrieser 2007). On Earth today, the magnitude of this biological flux is $\sim$0.4 Tmol yr^{-1} and includes contributions from both marine and terrestrial (including agricultural and industrial) sources (Tian 2015; Tian et al. 2020).

N_2O is of interest here because it produces notable features in Earth's near-IR (NIR) and MIR spectra (Sagan et al. 1993; Robinson & Reinhard 2018; Gordon et al. 2022). This, and its dominant biological origin on Earth, has led previous authors to consider N_2O as a potential remote biosignature for Earthlike planets, along with O_2, O_3, and CH_4 (Rauer et al. 2011; Grenfell 2017; Schwieterman et al. 2018). In general, previous studies of N_2O biosignatures have used present-day Earth's N_2O flux as a fiducial boundary condition to predict the resulting mixing ratios on an Earthlike planet orbiting another star or have used an inferred N_2O flux from Earth's geologic past as this surface boundary condition to predict mixing ratios to similar ends (Segura et al. 2003, 2005; Kaltenegger et al. 2007, 2020a; Rugheimer et al. 2013, 2015b; Grenfell et al. 2014; Tabataba-Vakili et al. 2016; Robinson & Reinhard 2018; Rugheimer & Kaltenegger 2018; Lin et al. 2021; Alei et al. 2022). Importantly, most of these past studies have typically predicted N_2O mixing ratios on exo-Earths that are lower or only modestly higher than modern Earth, leading to pessimistic predictions for N_2O detectability (e.g., Alei et al. 2022), though

it has long been recognized that low stellar UV fluxes promote N_2O accumulation (e.g., Segura et al. 2003, 2005; Grenfell et al. 2014; Rugheimer & Kaltenegger 2018) and that higher N_2O surface fluxes would result in a more detectable biosignature (Kaltenegger 2017; Schwieterman et al. 2018).

It has been hypothesized that biological fluxes of N_2O during the Proterozoic Eon (~2500–540 million years ago, Ma) may have been dramatically larger than at present, due to the limited availability of copper catalysts in euxinic (anoxic and sulfur-rich) oceans, which would have effectively short-circuited the last metabolic step in the denitrification cycle (Buick 2007; Figure 1). Higher atmospheric mixing ratios of N_2O could therefore also have contributed to greenhouse warming at the time (Roberson et al. 2011), although lower O_2 concentrations would have somewhat muted the impact of higher fluxes, due to the reduced shielding of photolyzing UV radiation (Roberson et al. 2011; Stanton et al. 2018). Under certain conditions, N_2O production on the earlier Earth could also have been augmented by chemodenitrification—that is, the process of N_2O production via abiotic reduction of nitric oxide (NO) by ferrous iron (Samarkin et al. 2010; Stanton et al. 2018). Previous studies have not comprehensively examined the full range of plausible N_2O fluxes over a range of pO_2 values and stellar types, including the end-member scenario, in which the nitrous oxide reductase enzyme that facilitates the last step in the denitrification process simply does not evolve (Pauleta et al. 2013). In such a scenario, we will show that N_2O can accumulate to high concentrations—even for planets orbiting FGK stars—with implications for the detectability of this biosignature gas with current and upcoming observatories.

Here, we conduct a systematic photochemical and spectral investigation of N_2O as an exoplanet biosignature and place upper limits on the N_2O abundances and detectability from a productive biosphere. In Section 2, we use the Earth system (biogeochemical) model "cGENIE" to calculate denitrification fluxes for an Earthlike marine biosphere as a function of atmospheric oxygenation levels (pO_2) and concentrations of bioavailable phosphorous (as PO_4^{3-}). We evaluate our results against literature values for the Earth and generate realistic bounds for plausible intermediate and maximum N_2O fluxes. In Section 3, we calculate the photochemical stability and steady-state mixing ratios of N_2O given a large range of fluxes, inclusive of those calculated in Section 2, with a variety of oxygenation states and for stellar hosts that span the main sequence (F4V to M8V). In Section 4, we generate emission and transmission spectra for a subset of the scenarios investigated in Section 3. Finally, we calculate the number of transits of TRAPPIST-1e that will be required to detect N_2O with JWST for three N_2O flux scenarios, and find that detecting N_2O with NIRSpec is plausible for production fluxes near the biospheric maxima. We discuss the implications and potential false positives in Section 5. We conclude in Section 6.

2. Circumscribing Plausible Global N_2O Fluxes with a Biogeochemical Model

To map out how the total oceanic denitrification (and hence the potential maximum N_2O production) rate varies as a function of pO_2 and phosphate availability (PO_4^{3-}), we use the cGENIE Earth system model of intermediate complexity. cGENIE consists of a 3D ocean circulation model plus a 2D energy balance and moisture model and a 2D sea-ice model. The 2D grid is split into 36×36 equal-area cells, while we

adopt 16 depth layers in the ocean, following Cao et al. (2009). cGENIE simulates a 3D marine biosphere, including phosphorous and nitrogen-limited primary production, and a set of metabolisms, including aerobic respiration, anaerobic respiration, methanogenesis, and aerobic methanotrophy (Ridgwell et al. 2007; Olson et al. 2016). A simple 2D (not vertically resolved) gridded calculation of basic atmospheric chemical reactions is also included (Reinhard et al. 2020). cGENIE has been leveraged to explore the coupled evolution of Earth's biosphere, atmosphere, and climate system over the entire geologic timescale, including the Archean (e.g., Olson et al. 2013), Proterozoic (e.g., Olson et al. 2016; Reinhard et al. 2016, 2020), and Phanerozoic (e.g., Kirtland Turner & Ridgwell 2016). cGENIE has most recently been used to explore the relationship between planetary obliquity, nutrient cycling, and the consequent potential for atmospheric oxygenation on exoplanets (Barnett & Olson 2022).

The biological N cycle in cGENIE includes diazotrophy (the biological reduction of N_2 to NH_4^+, which can then be incorporated into biomass), nitrification (the oxidation of NH_4^+ to NO_3^-), and denitrification (the biological reduction of NO_3^- to N_2). These processes are highlighted in Figure 1. Diazotrophy occurs only when N is scarce relative to phosphate (PO_4^{3-}) and N:P < 16 (the "Redfield Ratio") within the photic zone. Consequently, excess PO_4^{3-} availability relative to N will drive greater diazotrophy, until the global rates of N fixation balance N loss. The rates of nitrification and denitrification are both sensitive to atmospheric pO_2, which directly influences surface and benthic oxygen concentrations, but their relationships to oxygen differ dramatically. Nitrification requires O_2, whereas denitrification occurs in the absence of O_2. Denitrification additionally requires reduced organic material and is a multistep process, with several intermediate N species between NO_3^- and N_2, such as N_2O. The configuration of cGENIE employed here neglects this complexity and, by default, assumes the complete reduction of NO_3^- to N_2 when organic matter and NO_3^- are in sufficient abundance and local dissolved O_2 is low, following Naafs et al. (2019).

We estimate an upper bound on the possible N_2O flux arising from incomplete denitrification for a given atmospheric pO_2 and ocean nutrient inventory by assuming that the entire denitrification flux results in the evolution of N_2O (rather than going directly to N_2). This could occur, for instance, if the nitrous oxide reductase, the enzyme that facilitates the last step of the denitrification process (Pauleta et al. 2013), has not evolved or if dissolved copper, which is key to the functioning of this catalyst, was severely rate-limiting in abundance (Buick 2007). Nitrous oxide reductase can also be substantially inhibited in community settings by other biological products, including C_2H_2, CO, NO, N_3^-, and CN^- (Kristjansson & Hollocher 1980; Koutný & Kučera 1999). Our goal here is not to be overly prescriptive of the specific scenarios in which denitrification is incomplete, but instead to examine plausible maxima in N_2O production by Earthlike biospheres.

Figure 2 shows the total denitrification flux from Earth's marine biosphere as a function of pO_2 (relative to the present atmospheric level, or PAL) and phosphate availability (PO_4^{3-}, relative to the present ocean level, or POL). We simulate pO_2 levels of 0%–100% and phosphate availability between one and 2 times POL. The upper range of phosphate availability represents a planet with higher nutrient availability from enhanced continental weathering or a larger crustal abundance
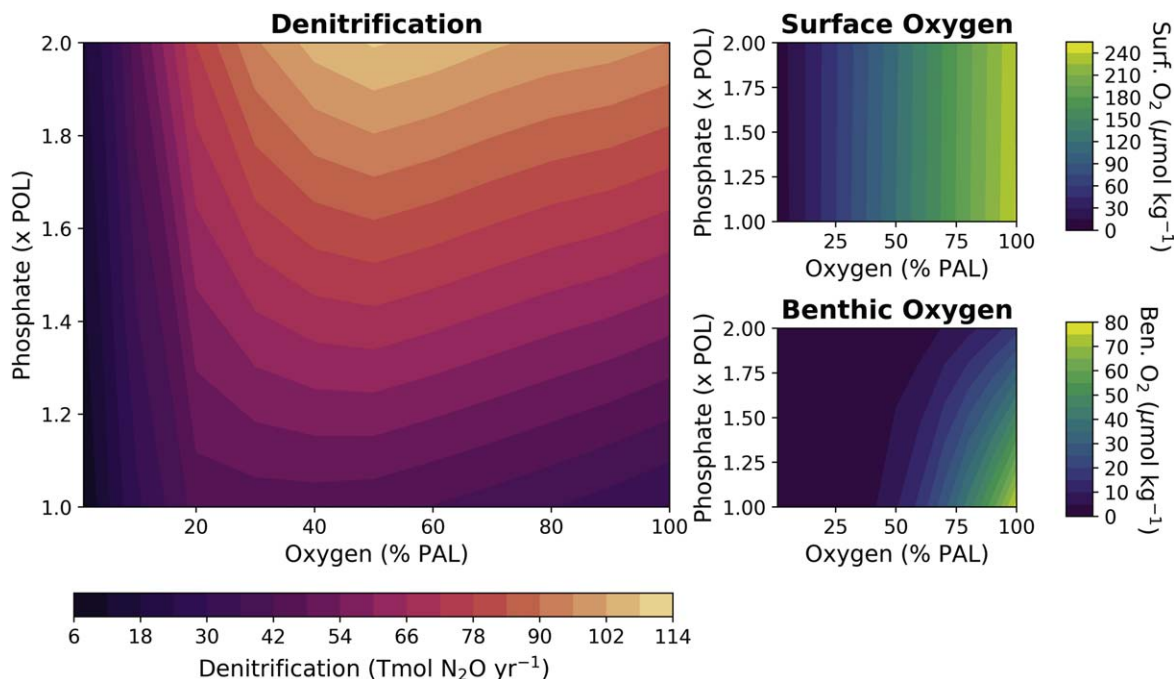
Figure 2. Results from GENIE showing (a) denitrification rates, (b) surface oxygen concentrations, and (c) benthic oxygen concentrations as a function of atmospheric oxygen (in terms of % of PAL; x-axis) and phosphate availability (in terms of POL; y-axis). Denitrification is optimized at intermediate atmospheric oxygen levels, where there is sufficient O_2 in the surface waters to stimulate surface nitrate production via nitrification, but insufficient O_2 to oxygenate the deep ocean, which would suppress denitrification.

of P compared to Earth. Continental weathering could be enhanced by a more robust hydrological cycle, greater topographic relief, or a larger extent of coastal depositional settings. Indeed, enhanced weathering in the wake of snowball deglaciation may have resulted in PO_4^{3-} concentrations transiently exceeding 2 times POL in the late Neoproterozoic, roughly coincident with the evidence for increases in oxygen levels (Planavsky et al. 2010). Steady-state P levels are unlikely to have dramatically exceeded ∼2 times POL at any point in Earth's history (Reinhard et al. 2017b; Lenton et al. 2018; Reinhard & Planavsky 2022).

The denitrification rates increase with P availability, which controls the organic C fluxes. The relationship between denitrification and atmospheric oxygen is more complex. At low levels of oxygen, nitrification, which requires oxygen, is limited. The denitrification rates are thus limited as well. At very high levels of oxygen, nitrification occurs readily, but denitrification, which requires low levels of oxygen, is suppressed. Oxygen is heterogeneously distributed in the ocean, such that both metabolisms may occur simultaneously, despite being spatially separated. Nitrification is favorable in well-oxygenated surface waters where oxygenic photosynthesis occurs, whereas denitrification is most favorable in oxygen minimum zones underlying productive regions of the surface ocean, where high organic C fluxes deplete O_2 via aerobic respiration. This possibility may be particularly true for atmospheric pO_2 that is lower than the present-day abundance.

Our results show a maximum denitrification flux of ∼40 Tmol yr^{-1} (1 × POL P) to 100 + Tmol yr^{-1} (2 × POL P) around an atmospheric pO_2 of ∼50% PAL O_2. At this intermediate oxygen level, the surface ocean is in equilibrium with the atmosphere and is well oxygenated, but the deep ocean remains poorly ventilated—optimizing the rates of both

nitrification and denitrification. However, the sensitivity to pO_2 is asymmetric around this level. At the lowest O_2 levels (<20% PAL), denitrification is strongly attenuated (due to limited nitrification; see, e.g., Anbar & Knoll 2002; Fennel et al. 2005). Toward higher O_2 levels, denitrification falls off, with a shallower linear decrease, as deep ocean oxygenation increases. However, even under very high oxygen levels, such as those of modern Earth, oxygen minimum zones persist and allow denitrification in an otherwise well-oxygenated ocean.

To contextualize our calculations, the total denitrification flux on modern Earth is about ∼20 Tmol N$_2$ yr^{-1}, with substantial uncertainties (Canfield et al. 2010). As shown in Figure 2, a planet with twice the nutrient P availability could maintain a denitrification flux of ∼100 Tmol yr^{-1} even at near-modern levels of O_2. This value is similar to a study of potential late Cretaceous (93 Ma) marine nitrogen cycling, for which Naafs et al. (2019) calculated a denitrification flux of ∼100 Tmol yr^{-1}, given 2 times POL, modern oxygen, and 4 times modern CO_2. We therefore adopt three fiducial N$_2$O fluxes in our subsequent photochemical calculations of N$_2$O abundances: 1, 10, and 100 Tmol yr^{-1}. A flux of 1 Tmol yr^{-1} represents 5%–10% of the global denitrification flux of modern Earth having evolved as N$_2$O rather than N$_2$, which is approximately a factor of 2 higher than Earth's estimated global N$_2$O flux (Tian et al. 2020). A flux of 10 Tmol yr^{-1} represents 50%–100% of the global denitrification flux of modern Earth (i.e., all NO_3^- that is consumed in denitrification becomes N$_2$O), while a flux of 100 Tmol yr^{-1} represents a global biosphere with lower oxygen and higher P than modern Earth, but consistent with periods of Earth's history. We regard the latter case as a reasonable upper bound for a weakly or fully oxygenated Earthlike world.

3. Calculating N_2O Abundances for FGKM Stars with a Photochemical Model

Here we test the N_2O flux–abundance photochemical relationships for a comprehensive range of N_2O fluxes, which include the bounds described above (1, 10, and 100 Tmol yr^{-1}), but also extend to much lower fluxes. Note that we do not explicitly distinguish fluxes from the ocean and fluxes from a terrestrial biosphere in our atmospheric calculations. For comparison, the total primary production of the land-based denitrification is about one half that of the ocean (with substantial uncertainty; see, for example, Falkowski et al. 2000; Gruber & Galloway 2008). This difference is relatively small in comparison to the increase in denitrification when increasing the oceanic P availability from 1 to 2× POL, and we thus consider plausible terrestrial fluxes to be broadly included within these original bounds.

3.1. Photochemical Model and Inputs

To calculate flux–abundance relationships for Earthlike planets as a function of N_2O flux and pO_2, we use the photochemical model component of the Atmos code[15] (Arney et al. 2016). The code was originally developed by Kasting et al. (1979) and has been improved by successive authors (Pavlov et al. 2001; Zahnle et al. 2006; Arney et al. 2016; Lincowski et al. 2018). The photochemical code uses the reverse Euler method to solve the flux and continuity equations at each vertical layer, providing stable solutions at steady state. The model uses a δ two-stream method to calculate the radiative transfer (Toon et al. 1989) and includes vertical transport via molecular and eddy diffusion. The atmosphere is divided into 200 layers of 0.5 km in altitude. The model contains NO production by lightning (Harman et al. 2018) and the H_2O cross-sectional and sulfur gas reaction rate updates recommended by Ranjan et al. (2020).

To enhance reproducibility, we use the publicly available Atmos "ModernEarthSimple" template. This template includes 50 species and 238 photochemical reactions and is appropriate for modeling major trace species (O_3, CH_4, CO, and N_2O) on high-oxygen Earthlike planets (e.g., Meadows et al. 2018a). Table 1 contains our assumed surface boundary conditions, including the deposition rates and volcanic fluxes. These boundary conditions are consistent overall with those of the modern Earth and those used in previous studies of O_2-rich planets (e.g., Segura et al. 2005; Schwieterman et al. 2019a, 2019b; Wunderlich et al. 2020). We assume a variety of O_2 abundances, ranging from 0.01–1.0 PAL, which is equivalent to 0.002 to 0.21 bar. Our N_2O surface fluxes range from 0.01 to 100 Tmol yr^{-1} (3.7×10^7 to 3.7×10^{11} molecules cm^{-2} s^{-1}). To further enhance reproducibility and isolate the sensitivity to varied molecular fluxes and stellar spectra, we assume a surface pressure of $P_0 = 1$ bar and a surface temperature of 288 K for all cases with Earth's modern temperature–pressure profile. N_2 is used as a filler gas. We compared our results to those obtained with the "ModernEarthComplex" template (based on Lincowski et al. 2018), which includes 71 additional reactions (309 total reactions) and 23 additional (73 total) chemical species, and found the predicted N_2O mixing ratios to be consistent between templates. We also examined the sensitivity to stratospheric

---

[15] https://github.com/VirtualPlanetaryLaboratory/atmos

Table 1
Photochemical Boundary Conditions

Chemical Species	Deposition Velocity (cm s^{-1})	Flux (Molecules cm^{-2} s^{-1})	Mixing Ratio
O	1	...	...
O_2	...	...	Variable
N_2	...	...	Variable
CO_2	5×10^{-5}	6.9×10^8	...
H_2O	...	...	Fixed[a]
H	1	...	...
OH	1	...	...
HO_2	1	...	...
H_2O_2	0.2	...	...
H_2	2.4×10^{-4}	...	...
CO	1.2×10^{-4}	3.0×10^{11}	...
HCO	1	...	...
H_2CO	0.2	...	...
CH_4	0	1×10^{11}	...
CH_3	1	...	...
NO	1.6×10^{-2}	1×10^9	...
NO_2	3×10^{-3}	...	...
HNO	1	...	...
H_2S	0.2	2×10^8	...
SO_2	1	9×10^9	...
H_2SO_4	1	7×10^8	...
HSO	1	...	...
O_3	0.07	...	...
HNO_3	0.2	...	...
N_2O	...	Variable	...
HO_2NO_2	0.2	...	...
OCS	0.01	1.57×10^7	...

Notes.
[a] The tropospheric H_2O profile is fixed to an Earth average (Manabe & Wetherald 1967).
[b] The species included in the photochemical scheme with a deposition velocity and flux of 0 include C_2H_6, HS, S, SO, S_2, S_4, S_8, SO_3, S_3, N, NO_3, and N_2O_5.

temperature profiles and found minimal differences that are small compared to our range of considered pO_2 levels, N_2O fluxes, and stellar spectra. Tropospheric temperature profiles should be relatively unaffected, assuming the same surface temperature of 288 K. Substantially different surface temperatures would impact H_2O abundances (depending on the relative humidity), which can have downstream impacts on CH_4 and other trace gases, but will have smaller influences on N_2O, given its major photochemical sinks (see below).

We sourced stellar spectra directly from the existing Atmos library, including the additions from Arney (2019). Figure 3 shows the stellar spectra used in our simulations, with the bottom panel zooming in on the UV component of each spectrum and the molecular cross sections for N_2O, O_2, O_3, and CH_4. Our solar spectrum was sourced from Thuillier et al. (2004). The original source of the spectrum for the star HD 85512 (K6V) is the Measurements of the Ultraviolet Spectral Characteristics of Low-mass Exoplanetary Systems treasury survey (Youngblood et al. 2016; France et al. 2016; Parke Loyd et al. 2018), and the original source for the Proxima Centauri (M5V) spectrum is the Habitable Zones and M dwarf Activity across Time program (Shkolnik & Barman 2014; Parke Loyd et al. 2018; Peacock et al. 2020). The TRAPPIST-1 spectrum was the median average from the three-activity models simulated by Peacock et al. (2019a, 2019b). Note that for TRAPPIST-1 and Proxima Centauri specifically, we adopted flux scaling consistent with TRAPPIST-1e and
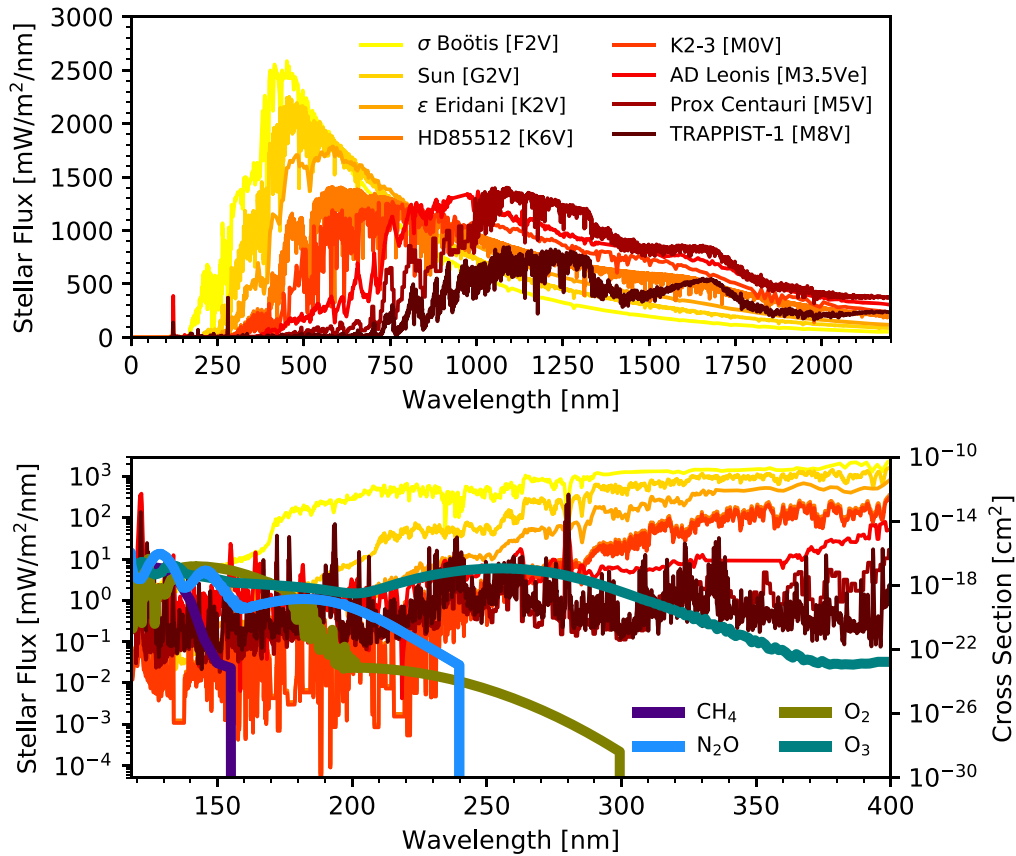
Figure 3. The top panel shows the stellar spectra used in our simulations. The bottom panel shows the UV wavelengths of the stellar spectra and the UV cross sections of N_2O, O_2, O_3, and CH_4 that are used in our simulations (the right y-axis).

Proxima Centauri b, while the other stars are scaled such that the simulated Earth-twin planet lies at the same Earth–Sun adjusted insolation value. However, the simulations using these scaling relationships are not meant to represent those planets precisely, since the surface gravity is not adjusted, and we do not account for potential synchronous rotation, to facilitate clear intercomparison of all photochemical results. For the case of the simulated transit spectra of TRAPPIST-1e, we adopted the planetary parameters, including surface gravity, that are described in Agol et al. (2021), and recalculated the photochemical results based on these values.

3.2. Predicted N_2O Flux–Abundance Relationships for FGKM Stars

Figures 4 and 5 show comprehensive flux–abundance relationships for N_2O as a function of the N_2O surface molecular flux and pO_2, using the modeling inputs described in Section 3.1 for Earthlike planets orbiting stars with spectral types F4V to M8V: Sigma Boötis (F4V), the Sun (G2V), Epsilon Eridani (K2V), HD 85112 (K6V), K2-3 (M0V), AD Leonis (M3.5V), Proxima Centauri (M5V), and TRAPPIST-1e (M8V). In addition to the colored shading that indicates the calculated N_2O concentrations, line contours are added to indicate the 0.1, 1.0, 10, 100, and 1000 ppm N_2O levels. Figure 6 shows the flux–abundance relationships for the 100% PAL (21% v/v O_2) cross section of this data for all stars. Figures 7 and 8 display a subset of this data in an alternative visualization format for $pO_2 = 100\%$ PAL (Figures 7) and $pO_2 = 50\%$ PAL (Figure 8). (We also provide the $pO_2 = 10\%$ PAL case in Appendix Figure A1).

From these photochemical flux–abundance simulations, we can observe that for a given star, the N_2O abundance is strongly dependent on the flux and only modestly dependent on the O_2 abundance (though we caution that the N_2O flux can be highly sensitive to pO_2, as shown in Figure 2). The predicted N_2O concentration is also very sensitive to the spectral type of the host star, with the largest enhancement seen for the late K dwarf HD 85112 (K6V) and the earliest M dwarf K2-3 (M0V). In comparison, σ Boötis (F4V) and the Sun (G2V) show the lowest N_2O buildup at any given N_2O surface flux (with σ Boötis being very slightly lower), while the mid-to-late M-dwarf planets maintain considerably higher N_2O concentrations than the Sun-like case at any given flux, but nonetheless maintain lower N_2O concentrations than the K-dwarf planets. The relationship between N_2O and O_2 is strongest for the F and G dwarfs, weaker for the M dwarfs, and weakest for the K6V and M0V stars, which maintain comparatively high N_2O at high fluxes, even for low O_2 levels.

These flux–abundance relationships result from the relative balance of photolysis and the other photochemical reactions that determine the atmospheric lifetime of N_2O. The major photochemical sink for N_2O is photolysis ($N_2O + h\nu \, [\lambda < 240 \, nm] \rightarrow N_2 + O(^1D)$), where photolysis proceeds most strongly via photons with wavelengths of less than 200 nm but weaker photolysis cross sections of up to 240 nm. Importantly, the wavelength-dependent overlap of the N_2O cross sections between different stellar hosts drives large differences in the estimated photolysis rates and, consequently, the photochemical lifetimes and estimated abundances (Figure 3). At a fixed surface molecular flux of N_2O, the trend of increasing N_2O
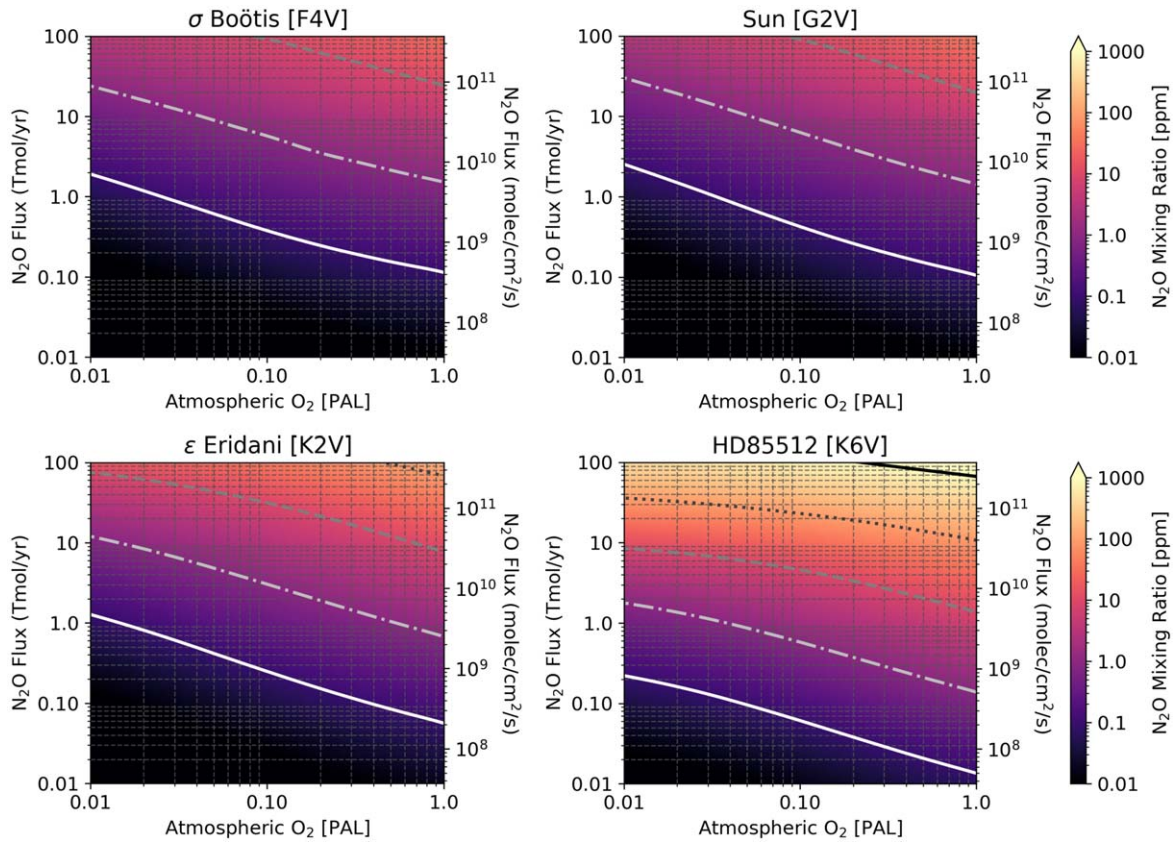
Figure 4. The atmospheric N_2O volume-mixing ratio (in ppm) as a function of atmospheric oxygen level in terms of PAL (x-axis) and the N_2O flux (y-axes). Each panel shows the results for an Earth analog at the inner edge of the habitable zone for Sigma Boötis [F4V], the Sun [G2V], Epsilon Eridani [K2V], and HD 85112 [K6V]. The solid white, light gray dotted–dashed, dark gray dashed, black dotted, and solid black lines represent 0.1, 1.0, 10, 100, and 1000 ppm N_2O contours, respectively. The surface boundary conditions are given in Table 1.

abundances as a function of pO_2 results from the shielding impact of the Schumann–Runge O_2 bands (175–195 nm) and, to a lesser extent, the ozone (O_3) Hartley band at longer wavelengths (200–310 nm). Larger oxygen concentrations result in greater O_2 shielding, enhancing N_2O lifetimes and abundances. Because this shielding is more directly reliant on O_2 shielding than O_3 (which is logarithmically dependent on O_2), the relationship between N_2O abundances and O_2 is smooth and largely linear in log–log space.

A consequential secondary photochemical sink for N_2O is the interaction with the $O(^1D)$ radical that can proceed through two channels: (1) $N_2O + (O^1D) \rightarrow N_2 + O_2$ and (2) $N_2O + O(^1D) \rightarrow NO + NO$. The $O(^1D)$ that reacts with N_2O can be sourced from N_2O photolysis, but for Sun-like host stars the substantially greater source is photolysis of the tropospheric ozone, via the reaction $O_3 + h\nu$ $(\lambda < 330 \, nm) \rightarrow O(^1D) + O_2$. This reaction channel is strongly dependent on a relatively narrow range of near-UV (NUV) photons that have sufficient energy to photolyze O_3, but are low enough in energy to avoid being absorbed by overlying O_2 and O_3 in the stratosphere before reaching the troposphere. These NUV photons are produced by the stellar photosphere, and so their flux is strongly dependent on the effective temperature of the host star (see Figure 3). Earthlike planets orbiting late-type stars are particularly poor generators of atmospheric $O(^1D)$ radicals (Segura et al. 2005; Grenfell et al. 2013, 2014; Rugheimer et al. 2015a; Arney 2019), and so this reaction channel is correspondingly weaker for K-host stars versus G-host stars, and weakest for M-dwarf stars. Our model also includes a

rainout sink for N_2O (Lincowski et al. 2018), which is a tertiary sink not dependent on stellar type.

The balance between the photolysis and $O(^1D)$ destruction channels is shown as a function of the surface N_2O mixing ratio for a subset of the stars examined in Appendix Figure A2. For all stars, photolysis causes the greatest loss rate for N_2O. For Sun-like G and F stars, reactions with $O(^1D)$ radicals are also a robust, though secondary, sink for N_2O. For the late K-dwarf stars, the $O(^1D)$ sink is intermediate between those for the G and M dwarfs, but the photolysis rate is the lowest among all possibilities. For M-dwarf stars, the $O(^1D)$ sink for N_2O is weak (Grenfell et al. 2013, 2014), but increased magnetic activity enhances the far-UV (FUV) radiation that can photolyze N_2O over relatively inactive K-dwarf stars. These photochemical loss relationships combine to put the latest K-dwarf hosts in the "sweet spot," with the lowest integrated N_2O loss rates over both types of photochemical sink, and hence the highest predicted concentrations at any fixed N_2O surface flux and pO_2 parameter combination.

We find that the FUV continuum has a crucial impact on the M-dwarf N_2O photolysis rates; it is only very weakly a function of the Lyα flux (Grenfell et al. 2014; Peacock et al. 2022), so the scaling or estimation of stellar spectra that do not account for the FUV continuum will yield divergent results from those presented here. This finding is consistent with the recent work of Teal et al. (2022), who focused on the impact of differences in the input stellar spectra on the signatures of CH_4 and haze on Archean-like planets. We note that models that artificially
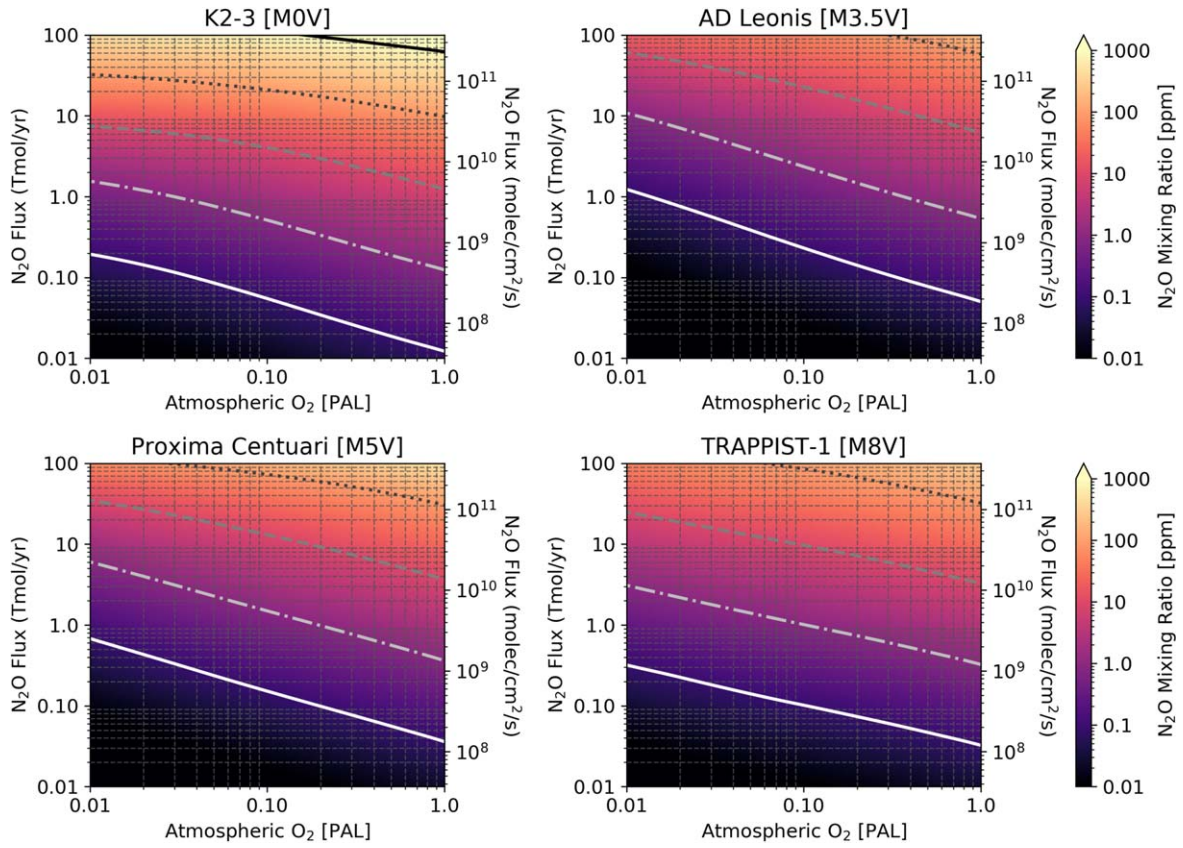
Figure 5. The same as Figure 4, but results are shown for Earthlike planets at the inner edge of the habitable zone of the M-dwarf stars K2-3 [M0V], AD Leonis [M3.5V], Proxima Centauri [M5V], and TRAPPIST-1e [M8V].
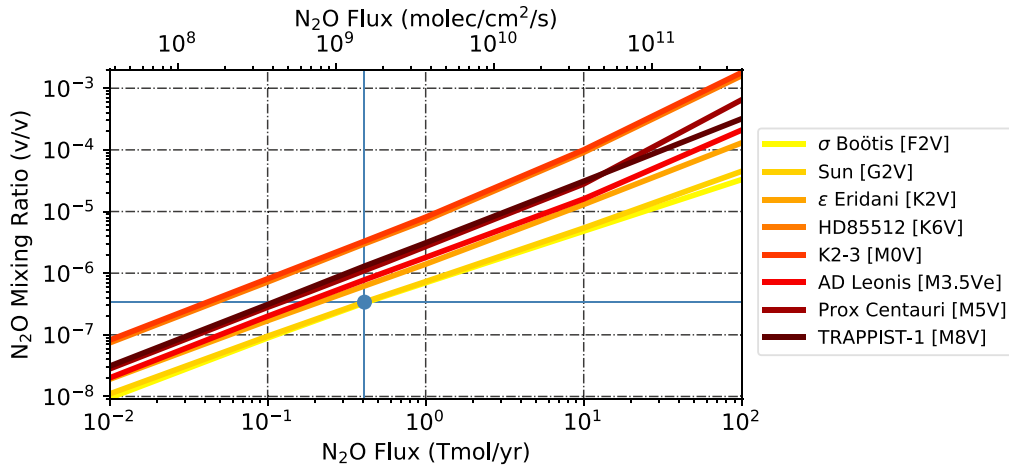

Figure 6. Atmospheric mixing ratios of N_2O as a function of the surface fluxes for an Earthlike atmosphere with $pO_2 = 100\%$ PAL. Results are shown for a range of stellar host stars (FGKM) and represent a vertical slice through the rightmost axis of the panels shown in Figures 4 and 5. The blue horizontal line shows the mixing ratios for N_2O in the modern atmosphere ($\sim$330 ppmv), while the blue vertical line indicates the modern N_2O surface flux ($\sim$0.4 Tmol yr^{-1} or 1.5×10^9 molecules cm^{-2} s^{-1}).

remove or substantially scale down the FUV continuum for M dwarfs (i.e., "inactive" stellar models) will instead show that inactive late M dwarfs, rather than late K dwarfs, produce the largest N_2O concentrations for a given flux, due to strongly attenuated N_2O photolysis (e.g., Grenfell et al. 2014; Rugheimer et al. 2015a). While modeling inactive M-dwarf photochemistry provides an informative sensitivity analysis, it is not representative of observed and modeled mid-to-late

M-dwarf spectra, which show substantial FUV continua (e.g., Peacock et al. 2019a, 2019b).

The flux–abundance relationships allow an estimation of the envelope of plausible N_2O concentrations given more or less efficient denitrification in exo-biospheres, where N_2O is evolved rather than N_2. For an Earth orbiting a solar twin (G2V), we find that N_2O fluxes of 10–100 Tmol yr^{-1} would lead to maximum N_2O abundances of 5–50 ppm for Earth–Sun
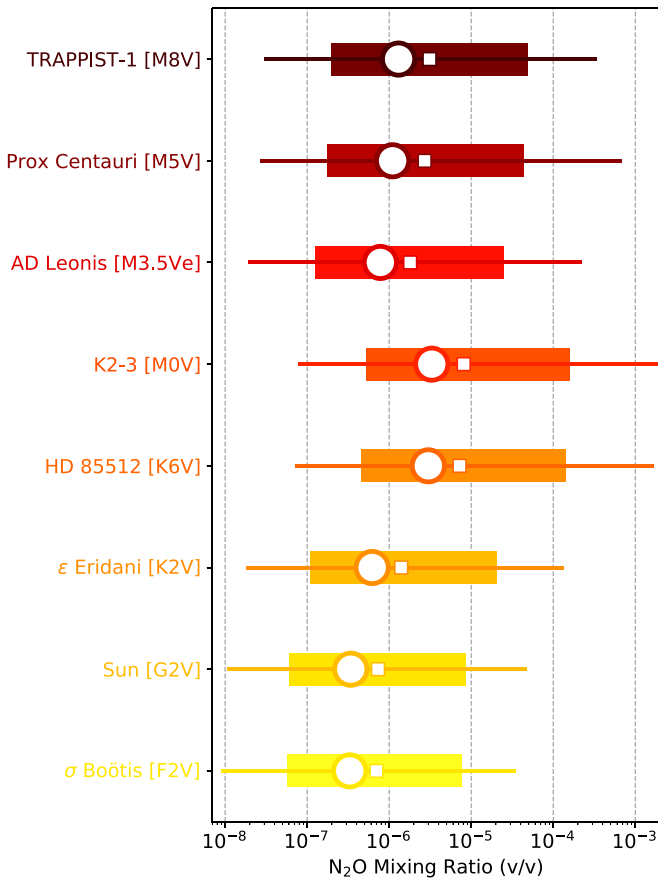
Figure 7. Steady-state ground-level mixing ratios of N_2O for modern Earthlike planets around a range of stellar hosts for an Earthlike planet with $pO_2 = 100\%$ PAL. The open circles show the results for a modern N_2O flux of ~ 0.4 Tmol yr^{-1} (1.5×10^9 molecules cm^{-2} s^{-1}), the open squares show the results for an N_2O flux of 1 Tmol yr^{-1}, the shaded bars show the range of 0.1–10 Tmol yr^{-1} (a factor of 10), and the horizontal lines show a range of 0.01–100 Tmol yr^{-1} (a factor of 100). A flux of 1 Tmol yr^{-1} corresponds to a surface molecular flux of 3.7×10^9 molecules cm^{-2} s^{-1}.

Figure 8. The same as Figure 7, but for an Earthlike planet with $pO_2 = 50\%$ PAL.

Appendix for more detailed descriptions of these sensitivity experiments.

3.3. Atmospheric Profiles for Spectral Simulations

We refined a subset of our flux–abundance calculations to prepare self-consistent chemical profiles as inputs for spectral simulations. We specifically consider an Earth–Sun scenario, an Earth orbiting HD 851512 (K6V), an Earthlike Proxima Centauri b, and an Earthlike TRAPPIST-1e. We adjust the surface gravities of Proxima Centauri b and TRAPPIST-1e so that they are consistent with values reported in the literature (Agol et al. 2021; Faria et al. 2022). Otherwise, we assume Earth's surface gravity ($9.8\ m\ s^{-2}$). For all scenarios, we calculate chemical profiles based on 1, 10, and 100 Tmol yr^{-1} N_2O surface fluxes. We continue to assume an Earthlike surface temperature of 288 K and a surface pressure of 1 bar. Figure 9 shows the resulting altitude-dependent chemical profiles for select trace gases (N_2O, O_3, CH_4, and CO). The N_2O profiles increase sensibly with flux, while the other trace gases, including CH_4, CO, and O_3, decrease with increasing N_2O flux. These decreases in trace gas abundance are primarily due to the increase in $O(^1D)$ radicals liberated by N_2O photolysis ($N_2O + h\nu$ [$\lambda < 240$ nm] $\rightarrow$ $N_2 + O(^1D)$). The $O(^1D)$ radicals directly or indirectly (e.g., via the downstream production of OH) attack trace gases, including CH_4, CO, and O_3. The O_3 is additionally destroyed via cycles catalyzed by NO, which is liberated from N_2O photolysis, and is thus strongly dependent on the N_2O abundance (Ravishankara et al. 2009). The magnitude of the impact of N_2O on other trace gases is inversely related to the photospheric

analogs, compared to ~ 330 ppb for modern Earth, given a surface N_2O molecular flux of ~ 0.4 Tmol yr^{-1}. The F4V dwarf stellar host σ Boötis tracks very closely to the Sun, with slightly lower N_2O mixing ratios for a given flux (see Figures 4 and 6). For the quiescent late K dwarf HD 85512 (K6V) and earliest M dwarf K2-3 (M0V), N_2O fluxes of 10–100 Tmol yr^{-1} would result in N_2O mixing ratios of 90–1600 ppm. This is important, because N_2O concentrations are increased by about two orders of magnitude for a given flux for an exo-Earth orbiting a late K-dwarf star versus a solar analog. Indeed, the modern N_2O flux on Earth would result in N_2O concentrations of ~ 3 ppm for Earth analogs orbiting these host stars, compared to the 330 ppb modern N_2O concentration. We note that these N_2O concentration envelopes are most applicable to planets with Earthlike instellations and Earthlike CO_2 values. Habitable planets that are located in the outer habitable zone will experience lower UV fluxes, reducing the major sink of N_2O, and gain additional CO_2 shielding, assuming that CO_2 is the major greenhouse gas.

We tested the sensitivity of our results to different N_2 partial pressures (Figure A3) and increases in assumed eddy diffusion (Figure A4). In general, the trends described here are robust to large changes in these variables. We direct the reader to the
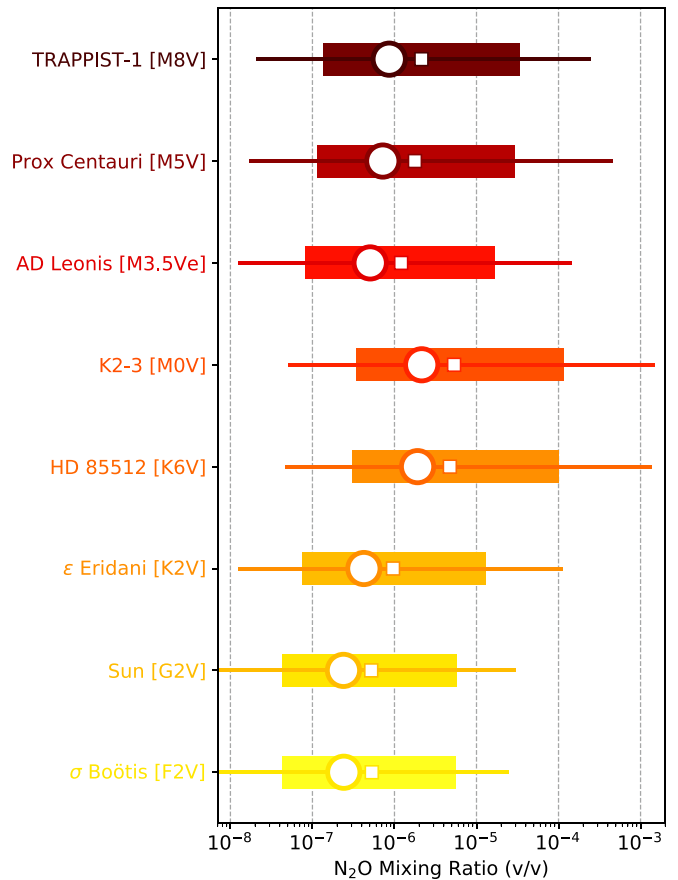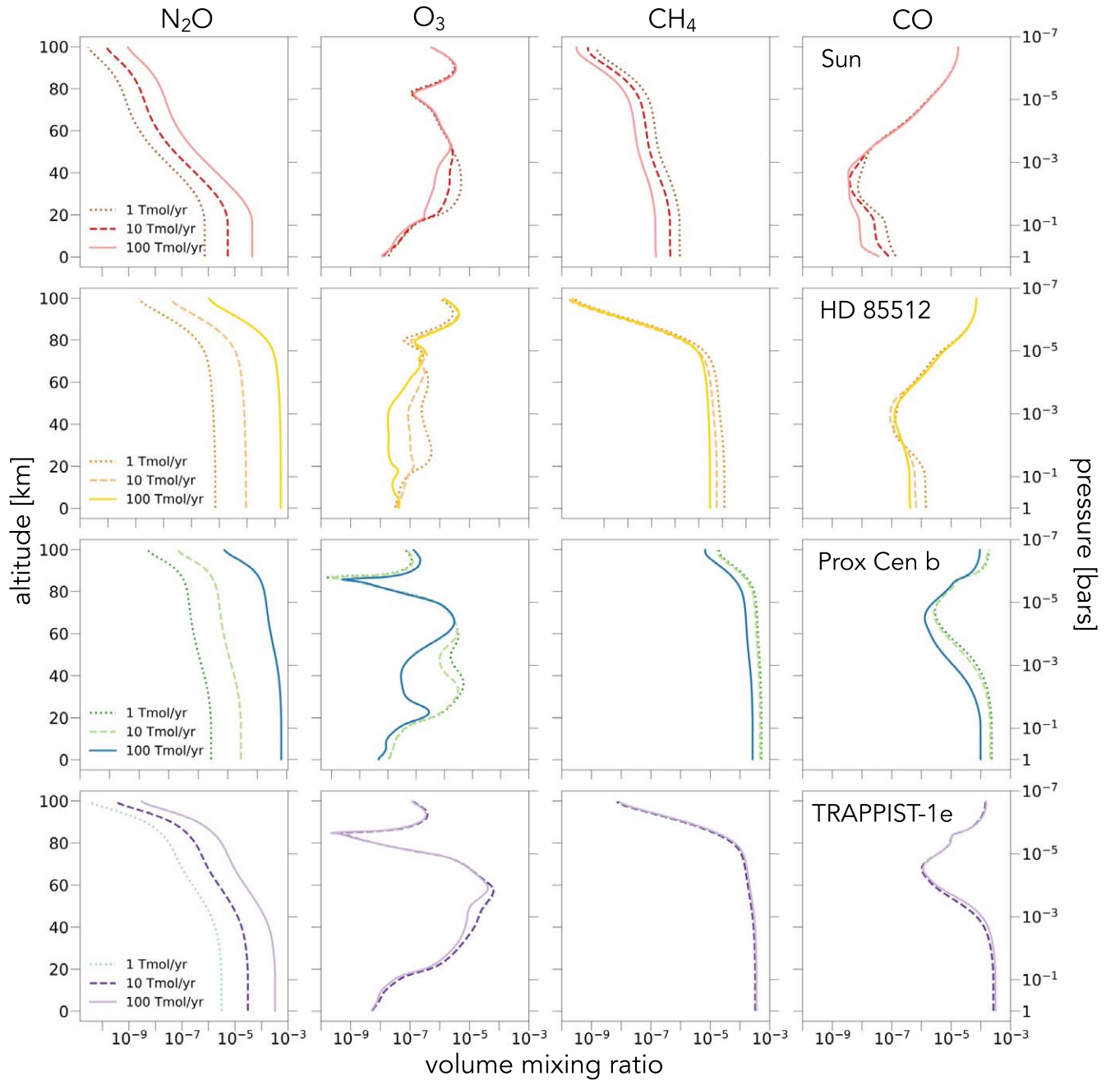
Figure 9. Gas mixing ratio profiles for (from top to bottom): the Earth orbiting the Sun, an Earthlike planet orbiting the late K-dwarf star HD85512 (K6V), an Earthlike Proxima Centauri b, and an Earthlike TRAPPIST-1e. The N_2O profiles assuming fluxes of 1, 10, and 100 Tmol yr^{-1} are shown. For brevity, not all species are included. All runs assume $pO_2 = 100\%$ PAL.

temperature of the host star, and is particularly muted in the TRAPPIST-1e case. Note that while increasing the N_2O fluxes leads to less abundant CH_4, the overall CH_4 mixing ratios are considerably higher for the M-dwarf planets than for the G- or K-dwarf planets, as expected (Segura et al. 2005; Rugheimer et al. 2015a).

4. N₂O Observables in the NIR and MIR

4.1. Spectral Simulation Tool

We use the Planetary Spectrum Generator (PSG) to simulate emission and transmission spectra of select cases that are explored in Section 3. PSG is a versatile and publicly accessible radiative transfer tool that is used to simulate remote observables for a wide variety of planetary objects and viewing geometries, which can calculate synthetic noise for a variety of instrumental configurations (Villanueva et al. 2018, 2022). The input IR opacities of PSG are sourced from the HITRAN database (Gordon et al. 2022). PSG has been widely used for the forward modeling of planetary spectra and the calculation of anticipated noise sources, particularly the cases of terrestrial exoplanetary atmospheres (Fauchez et al. 2020; Suissa et al. 2020; Pidhorodetska et al. 2020, 2021).

4.2. Simulated Thermal Emission Spectra

We used PSG to calculate synthetic thermal emission spectra from 5 to 20 μm for planets with the chemical profiles shown in
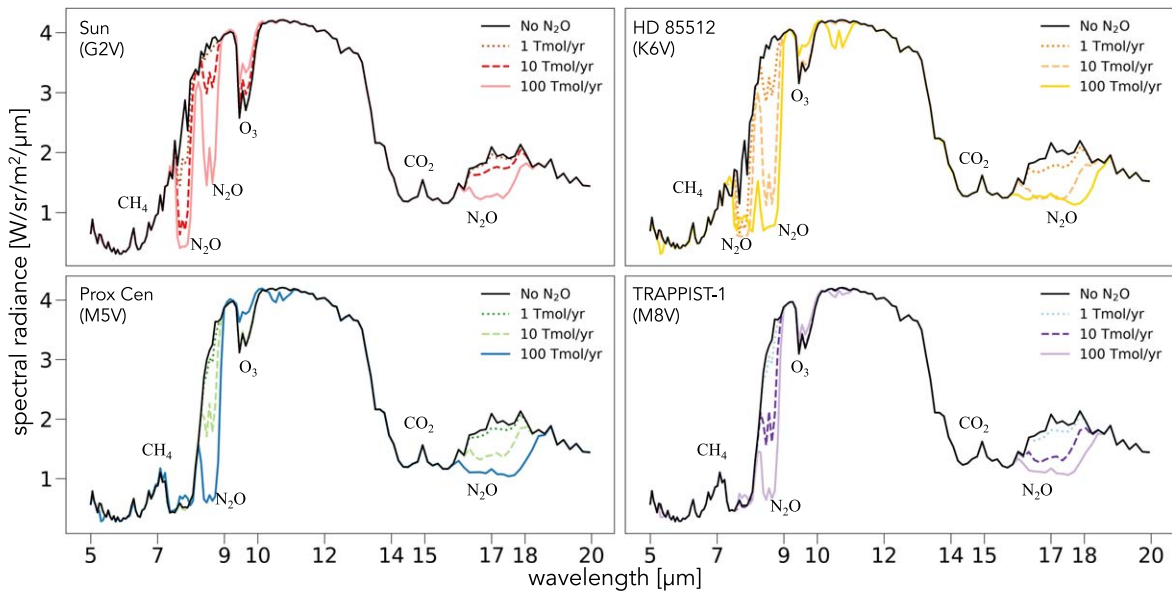
Figure 10. Simulated thermal emission spectra of (a) an Earth–Sun scenario, (b) an Earth orbiting the late K-dwarf star HD85512 (K6V), (c) an Earthlike Proxima Centauri b, and (d) an Earthlike TRAPPIST-1e. Each figure shows variations in the spectra according to N_2O surface fluxes of 1, 10, and 100 Tmol yr^{-1}, using the temperature and gas mixing ratio profiles shown in Figure 9 and assuming 50% cloud cover.

Figure 9. We assumed 50% cloud cover for all cases, with half liquid water cloud particles and half cirrus cloud particles. Planetary thermal emission spectra could be targeted by future space-based interferometers, such as the LIFE mission concept (Quanz et al. 2018, 2019, 2022; Defrère et al. 2018; Alei et al. 2022). Direct imaging in the thermal IR is also a possibility for a handful of systems with ground-based 30 m class telescopes (Fujii et al. 2018; López-Morales et al. 2019). We did not attempt to quantify the relative detectability of the features modeled in emission, since the parameters and capabilities of these future observations are not yet well defined. However, we note that these simulations will be useful inputs for future ground- and space-based thermal IR detectability studies.

Figure 10 shows indicative planetary thermal IR spectra of four scenarios: (1) an exo-Earth orbiting a solar twin; (2) an exo-Earth orbiting the K6V star HD 85512; (3) an Earthlike Proxima Centauri b; and (4) an Earthlike TRAPPIST-1e. These scenarios are hypothetical in nature and likely do not represent the actual planets, but are self-consistent representations of modern O_2-rich Earthlike worlds orbiting stars of similar spectral type. Each scenario shows the resulting spectra for no N_2O flux and for N_2O surface fluxes of 1, 10, and 100 Tmol yr^{-1}. The major N_2O bands in the thermal IR have band centers at 7.8, 8.5, and 17 μm. Among these, the 8.5 μm band has the highest intrinsic opacity (Gordon et al. 2022). As anticipated, the depths of these absorption bands are a strong function of surface flux and the host star spectrum. The strongest N_2O bands at a given flux are seen for the K6V host, while those for the hypothetical Earthlike Proxima Centauri b and TRAPPIST-1e are markedly greater at each given flux than those for the Earth–Sun scenario.

For the exo-Earth orbiting the K6V host, N_2O absorption bands become comparable to other biosignature absorption features, such as O_3 at 9.65 μm, at an N_2O surface flux of only 1 Tmol yr^{-1} (around 2.5 times the modern Earth's globally averaged N_2O flux). For N_2O surface fluxes of 1–10 Tmol yr^{-1}, N_2O bands become comparable to O_3 for the Proxima Centauri b and TRAPPIST-1e cases. For the Earth–

Sun scenario, N_2O surface fluxes must be above 10 Tmol yr^{-1} for the absorption depth of the 8.5 μm N_2O band to become comparable to the 9.65 μm O_3 band. At 100 Tmol yr^{-1}, an additional but intrinsically weak band of N_2O becomes noticeable for the K6V case centered at 10.6 μm. This may be a particularly useful diagnostic of extremely high N_2O fluxes, comparable to the anticipated denitrification flux of the entire planetary biosphere.

From the spectra plotted in Figure 10, interactions between the detectability of biosignature gases become notable. The depth of the 9.65 μm O_3 band is strongly influenced by the N_2O flux for the Earth–Sun case, which has somewhat less of an effect for the K6V and M5V scenarios, and a minimal effect for the TRAPPIST-1 case. These observations are consistent with the depletions in chemical profiles calculated as inputs in Figure 9, as discussed in Section 3.3. Importantly, the 7.8 μm N_2O band is obscured in the Proxima Centauri b and TRAPPIST-1e atmospheres by the 7.7 μm CH_4 band. The methane is substantially more abundant in these atmospheres at a given flux than in the G- or K-dwarf planets; however, the N_2O abundance could still be estimated from the 8.5 μm N_2O band, which is not substantially contaminated by CH_4 absorption.

We emphasize that the MIR spectral results presented here differ from previous work primarily because we consider the potential for larger biogenic N_2O fluxes, informed by our biogeochemical model, rather than a fundamentally different treatment of photochemistry or spectral simulation. For example, Rugheimer & Kaltenegger (2018) predicted biosignature abundances, including N_2O, based on biological fluxes inferred from Earth–Sun mixing ratios, including those estimated for Earth's earlier geologic epochs. The N_2O mixing ratios for earlier Earth eons were estimated to be lower than those of the present day ($\sim$0–100 ppb), because of less efficient UV shielding due to lower atmospheric oxygen concentrations, but with biogenic N_2O fluxes that are similar to those of Earth today. Consequently, Rugheimer & Kaltenegger (2018) find that, given these assumptions, N_2O does not contribute notably
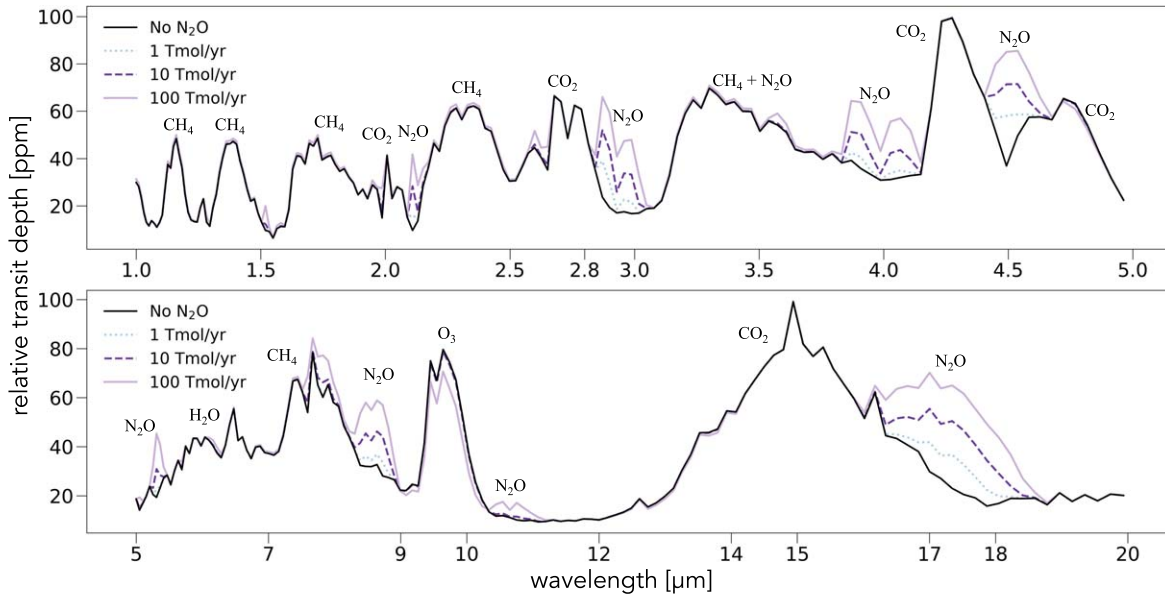
Figure 11. A simulated transmission spectrum of TRAPPIST-1e with N_2O surface fluxes of 1, 10, and 100 Tmol yr^{-1}, assuming the same gas profiles as shown in Figure 8(d), simulated with PSG. Major spectral features are noted. The top panel shows wavelengths accessible to the JWST NIRSpec instrument, while the bottom panel shows wavelengths accessible to the JWST MIRI instrument.

to the emitted light spectrum, and would likely be undetectable in a low-resolution and photon-limited exoplanet spectrum for each case that they investigated. We note that those cases assume an N_2O signature that is smaller than those we estimate for the 1 Tmol yr^{-1} case presented in Figure 10, and so our overall results are comparable when comparing equivalent N_2O fluxes and oxygen concentrations.

4.3. TRAPPIST-1e Transit Test Case with JWST

We used PSG to simulate the NIR and MIR transmission spectra of our Earthlike TRAPPIST-1e and to determine the number of transits necessary to detect N_2O with the JWST NIRSpec configuration. When calculating transmission spectra, we adopt the TRAPPIST-1e atmospheric profiles shown in Figure 9 and the planetary parameters in Agol et al. (2021).

Figure 11 shows the simulated transmission spectrum of the Earthlike TRAPPIST-1e with surface N_2O fluxes of 0, 1, 10, and 100 Tmol yr^{-1} from 1 to 20 μm. The bottom panel of Figure 11 is directly comparable to the emission spectrum of TRAPPIST-1e from Figure 10, showing the complementarity of these two observing modes. The major bands in the NIR are located at 2.25, 2.9, 4.0, and 4.5 μm, with relatively weaker bands at 1.5, 1.6, 1.7, 1.8, 2.6, and 3.7 μm. The overlap with the CH_4 absorption strongly attenuates the impacts of many of these bands, so their impacts on the transmission spectra are not entirely the result of their intrinsic opacities, but also the overlap with the CH_4 bands centered at 1.4, 1.7, 2.3, and 3.4 μm. At a modest N_2O flux of 1 Tmol yr^{-1}, features are only apparent at 2.1, 2.9, 4.0, and 4.5 μm. At N_2O fluxes of 10–100 Tmol yr^{-1}, the relative transit depths of these bands become comparable to those of CH_4 and CO_2. The major bands in the MIR transmission spectrum are at 7.8, 8.5, and 17 μm. As in the emission spectrum, the 7.8 μm band is effectively hidden by the 7.7 μm CH_4 band. Also, as seen in the emission spectrum, the 9.65 μm O_3 band becomes truncated, due to more efficient photochemical destruction in the highest N_2O flux case.

Table 2
JWST Detectability Calculations for N_2O Flux Scenarios

Flux Case	Feature (μm)	Transits for 3σ	Transits for 5σ
1 Tmol yr^{-1}	2.10–2.16	>1000	>1000
	2.86–2.97	148	409
	3.89–4.09	>1000	>1000
	4.47–4.52	212	587
10 Tmol yr^{-1}	2.10–2.16	140	388
	2.86–2.97	35	97
	3.89–4.09	109	303
	4.47–4.52	81	223
100 Tmol yr^{-1}	2.10–2.16	36	98
	2.86–2.97	13	36
	3.89–4.09	25	68
	4.47–4.52	41	114

We calculate the detectability of the NIR N_2O bands with JWST for all cases. We use the PSG JWST instrument simulation for the NIRSpec Prism to calculate the signal-to-noise ratio (S/N) for each major band, and subsequently calculate the number of transits needed to achieve an S/N ratio sufficient for detection to 3σ and 5σ. We add out-of-transit noise, using a transit to out-of-transit time ratio of 1:3, which lowers the S/N by a factor of ~1.16. This ratio was selected to match the planned observations of TRAPPIST-1e with JWST (JWST GTO program 1331; Lewis et al. 2017). Our tabulated detectability estimates are given in Table 2 for the bands centered at 2.1, 2.9, 4.0, and 4.5 μm.

We find that for fluxes of 10–100 Tmol yr^{-1}, N_2O is plausibly detectable on TRAPPIST-1e (assuming that it is an Earthlike world). For example, considering a flux of 100 Tmol yr^{-1}, the 2.9 μm band of N_2O would be detectable to 3σ in 13 transits and 5σ in 36 transits. Given a flux of 10 Tmol yr^{-1}, N_2O could be detectable at 3σ in 35 transits. We find that N_2O is not likely to be detectable for fluxes around or less than 1 Tmol yr^{-1}, consistent with previous results (Wunderlich et al. 2019). Figure 12 shows our 100 Tmol yr^{-1} TRAPPIST-1e scenario with realistic noise from PSG for 40
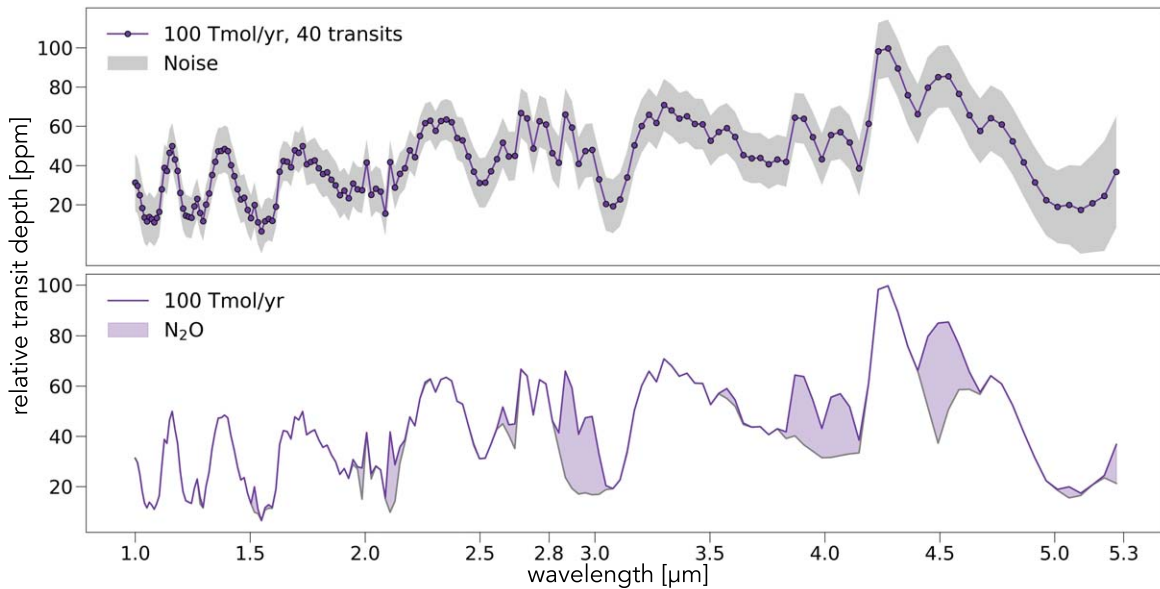
Figure 12. A simulated transmission spectrum of the Earthlike TRAPPIST-1e case, with a flux of 100 Tmol yr^{-1} N$_2$O. The top panel shows simulated 5σ error envelopes, as calculated with PSG, assuming 40 coadded transits with the JWST NIRSpec instrument. The bottom panel shows the influence of N$_2$O on the spectral features of the top panel.

transits. The gray shaded area indicates the 3σ noise envelope, while the bottom panel illustrates the selective impact of N$_2$O on the planetary spectrum.

We considered the detectability of the 7.8 and 8.5 μm bands with the MIRI-LRS instrument, but found that the number of transits to detect even the 100 Tmol yr^{-1} case at 5σ exceeded the nominal five-year mission lifetime of JWST (results not shown). We also considered the detectability of all bands with Origins MISC-T, but did not find a notable advantage over JWST NIRSpec in the NIR or JWST MIRI-LRS in the MIR (results not shown).

As was the case for the simulated MIR spectra presented in Section 4.2, the primary difference between the N$_2$O transmission signatures that we predict here and the estimates from other researchers simulating synthetic transmission spectra of Earthlike planets with N$_2$O (e.g., Wunderlich et al. 2019, 2021) is due to our consideration of larger potential biogenic fluxes. A globally averaged Earth flux applied to TRAPPIST-1e would result in the N$_2$O spectral features falling below the 1 Tmol yr^{-1} spectrum in Figure 11.

5. Discussion

5.1. Possible N$_2$O Flux Regimes

Our results demonstrate that the detection of N$_2$O on O$_2$-rich terrestrial exoplanets is plausible in the near-to-intermediate future for scenarios where the N$_2$O flux approaches 5%–10% of the modern Earth's global denitrification flux or greater. How likely is this to happen? It is difficult to extrapolate from one data point, but both the energetics of nitrogen metabolism and the biogeochemical evolution of Earth's oceans and atmosphere both suggest that such a scenario is very possible.

In the extreme case, life on an exoplanet may not have evolved the nitrous oxide reductase enzyme that facilitates the last step of the denitrification process (N$_2$O → N$_2$). This step, while thermodynamically favorable, has the highest kinetic barrier (Pauleta et al. 2013; Carreira et al. 2017), so it is less evolutionary advantageous to evolve this step instead of any

other. We have demonstrated that the atmosphere of a planet with even a maximally productive biosphere would not become dominated by N$_2$O, due to the efficiency of N$_2$O photolysis. In effect, the last step of the denitrification cycle (N$_2$O → N$_2$) on such a planet would be accomplished abiotically, via photolysis, and the atmosphere would never be placed into a chemical runaway (Ranjan et al. 2022). However, we have found that the N$_2$O concentrations of such a world would be high compared to those of present-day Earth—between tens and thousands of ppm N$_2$O, depending on the host star.

An N$_2$O concentration this high would constitute a large unexploited chemical disequilibrium. An unexploited disequilibrium can be interpreted as a biosignature or antibiosignature, depending on the context (Wogan & Catling 2020). In this case, N$_2$O concentrations of tens or even thousands of ppm are not conceptually different from the unexploited equilibria on Earth today and in the geologic past—the result of a highly productive photosynthetic biosphere. For example, CH$_4$ is out of equilibrium with O$_2$ on Earth, which has long been interpreted as a biosignature (Lovelock 1965, 1975; Hitchcock & Lovelock 1967). (It is not kinetically efficient for life to pull large amounts of CH$_4$ out of the atmosphere to react with O$_2$, even though it is thermodynamically favorable.) Methane on the Archean Earth was out of equilibrium with the CO$_2$ in the atmosphere (Krissansen-Totton et al. 2018), and the CH$_4$ concentrations on Archean Earth may have been in the range of hundreds to thousands of ppm or greater (Arney et al. 2016; Olson et al. 2018a; Robinson & Reinhard 2018), which is comparable to the maximum N$_2$O concentrations that we find here.

Even if the nitrous oxide reductase enzyme (or its analog) had evolved on an exoplanet, N$_2$O fluxes may still be high, depending on the environmental context. Trace nutrient limitation may impact the viability of biological N$_2$O reduction to N$_2$, which likely depends on enzymes (as it does on Earth). As an example, the nitrous oxide reductase enzyme requires copper catalysts (Carreira et al. 2017), and if copper were sharply limited, a much greater proportion of the total

denitrification flux would be released into the atmosphere as N_2O versus N_2. The initial copper inventory may be limited on an exoplanet compared to Earth, based on the balance of pebble and planetary accretion to larger impacts (Mahan et al. 2018) or the scatter in stellar metallicities (Delgado Mena et al. 2017). Alternatively, widespread ocean euxinia (simultaneous anoxia and elevated levels of H_2S in the water column) could dramatically lower the availability of copper as a micronutrient, which has been proposed for the earlier periods of Earth's evolutionary history (Buick 2007). Euxinic oceans are more likely to occur at lower oxygen levels, which work against N_2O lifetimes and, by extension, predicted abundances. However, euxinic environments are not completely unknown even on Earth today (Lyons & Severmann 2006), and they could be more extensive on a well-oxygenated exoplanet, given different balances between volcanic sulfur (H_2S) fluxes, ocean volumes, and the number and nature of anoxic basins. Moreover, intermediate oxygenation states of 20%–50% PAL would both favor euxinia and maximize denitrification fluxes, while conferring only a modest impact on N_2O lifetimes, due to reduced O_2 shielding. The photolysis dependence of N_2O on O_2 levels is substantially reduced for late K- and M-dwarf hosts versus Sun-like F, G, and early K hosts, so lower O_2 levels will be less impactful on N_2O abundances for the planets orbiting these stars.

Other planetary environmental conditions may impact N_2O production, including pH effects (Chen et al. 2015). The ocean pH of planets in the habitable zone may vary over a wide range, encompassing acidic (pH < 7) as well as basic (pH > 7) ocean chemistries, based on the required CO_2 to maintain clement conditions and equilibrate the carbonate-silicate thermostat (Schwieterman et al. 2019b; Krissansen-Totton & Catling 2020). Planetary environmental conditions may impact the community composition of the organisms that are involved in the nitrogen cycle, which will affect the production and loss of biological or abiotic products that can have an inhibitory impact on nitrous oxide reductase, such as CO, CN^-, I^-, C_2H_2, and N_3^- (Kristjansson & Hollocher 1980; Koutný & Kučera 1999; Paraskevopoulos et al. 2006). An important task moving forward will be to more definitively evaluate the conditions of ocean biogeochemistry that would be most likely to lead to elevated N_2O fluxes, and to establish how widespread these might be for habitable worlds.

We briefly note that agricultural activity has resulted in enhanced production of fixed nitrogen on Earth, which has in turn increased the rate of terrestrial N_2O production (Tian et al. 2020). Haqq-Misra et al. (2022) proposed that anomalously high NH_3, N_2O, and CH_4 in combination may serve as a "technosignature" for extensive planetary agriculture, and applied this concept to various scenarios for future population growth on Earth. Our results suggest a substantial overlap between the predicted N_2O flux and mixing ratios for robust agriculture and an ocean biosphere where a large fraction of the denitrification flux is released as N_2O. However, we do not predict that this would lead to a simultaneous evolution of NH_3, which underpins the arguments in Haqq-Misra et al. (2022). Moreover, our predicted photochemical flux–abundance relationships for FGKM stars can be applied to modeled agricultural production of N_2O, and could therefore inform future studies similar to that of Haqq-Misra et al. (2022).

Ultimately, a robust production flux of N_2O is essential for both the practical considerations of detectability and our ability to infer an explicit link to biological production, since abiotic processes can produce N_2O at low levels (e.g., Schumann & Huntrieser 2007; also see the text below). To rule out processes that may generate false positives, all biosignature gases, including N_2O, must be evaluated in terms of the planetary context (Meadows et al. 2018b; Krissansen-Totton et al. 2022). Figure 13 is a concept graphic that illustrates planetary scenarios in which N_2O can either be interpreted as a biosignature or ruled out as a clear biosignature, given the planetary context or other complementary spectroscopic observables. We discuss these scenarios in detail in the subsections below.

5.2. Stellar Activity and False Positives

Stellar activity and solar proton events (SPEs) have long been known to produce NO in Earth's atmosphere, via the secondary production of energetic electrons (Crutzen et al. 1975). These NO precursors could be a potential source of abiotic N_2O in some planetary atmospheres with sufficient H-bearing species, via the reaction $NO + NH \rightarrow N_2O + H$ (Airapetian et al. 2016, 2020). Airapetian et al. (2016) found that N_2O could have been generated at the ppb level on the anoxic and weakly reducing Hadean Earth by a younger, more active Sun. An active Sun would produce substantially higher fluxes of energetic protons and electrons, which can split N_2 into N in the upper atmosphere (normally the photolysis of N_2 is limited by the paucity of solar photons energetic enough to break the $N \equiv N$ triple bond). Subsequent photochemical reactions can produce N_2O, e.g., $N(^4S) + NO_2 \rightarrow N_2O + O$, in addition to $NO + NH \rightarrow N_2O + H$. More recent refinements to this model have predicted ground-level N_2O concentrations as high as ~ 1 ppm and stratospheric concentrations as high as ~ 1000 ppm, which could have had notable impacts on the Hadean or early Archean climate (Airapetian et al. 2018, 2020). The highest predicted (column-integrated) abundances are comparable to those of our 1–10 $Tmol\,yr^{-1}$ models.

How could we distinguish between biological N_2O and N_2O that is generated from stellar SPEs? The characterization of the host star is essential. A critical consideration is whether the star is young and magnetically active, presenting qualities associated with SPEs and coronal mass ejections (CMEs), which may be indicated by EUV and X-ray and extreme-ultraviolet (XUV) flares (Hu et al. 2022). A star with similar activity to the modern Sun will not produce meaningful abiotic atmospheric N_2O. Older, less magnetically active stars are also more enticing targets from the perspective of life detection, due to the additional time allowed to evolve a complex biosphere (Turnbull & Tarter 2003). The characterization of the host star required for this activity is likely to be less onerous than the detection of biosignature gases in orbiting terrestrial planets. Forward ion photochemical modeling, such as that performed by Airapetian et al. (2016), can make predictions of the abiotic N_2O generation potential, given observed time-dependent stellar inputs. Finally, age and activity estimates for nearby Sun-like stars with directly imageable habitable zones are known (Turnbull & Tarter 2003; Reid et al. 2007; Turnbull 2015), with most being $> \sim 3$ Gyr or older, and therefore less likely to be active and plausible candidates for efficient abiotic production of N_2O on orbiting terrestrial planets.

Spectral discriminants, such as HCN, could also be used to fingerprint the abiotic generation of N_2O in weakly reducing anoxic atmospheres that contain CH_4. The photochemical
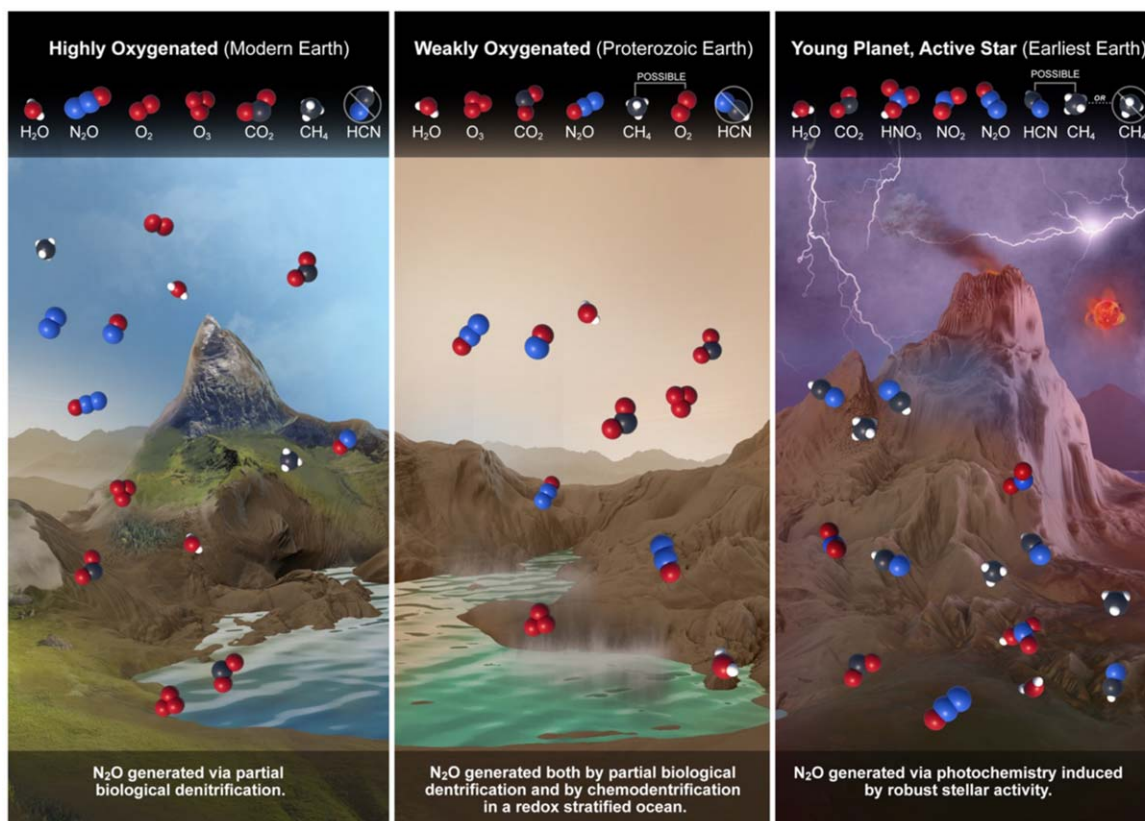
Figure 13. A concept image illustrating the interpretability of N_2O as a biosignature in the context of the planetary environment. The left panel illustrates a scenario like the modern Earth, with a high-oxygen atmosphere and N_2O generated overwhelmingly via partial biological denitrification. In this case, the simultaneous presence of O_2, O_3, N_2O, and CH_4 indicates a strong chemical disequilibrium. The middle panel illustrates a weakly oxygenated planetary environment like the Proterozoic Earth, with N_2O generated both by partial biological denitrification and by chemodenitrification of nitrogenous intermediates (likely substantially biogenic) in a redox stratified ocean. In this case, molecular oxygen (O_2) and methane may have concentrations that are too low to detect directly, but detectable N_2O and O_3 would be a strong biosignature. A false positive is unlikely, because an abiotic O_2 atmosphere would be unstable in combination with a reducing ocean. The right panel illustrates the most likely false-positive scenario, where an active star splits N_2 via SPEs, resulting in photochemically produced N_2O. This scenario would predict additional photochemical products, such as HCN, that would be indicative of abiotic origins. Stellar characterization would confirm the magnitude of the stellar activity. Vigorous atmospheric production of NO_x species could be inferred from spectrally active NO_2.

modeling of abiotic N_2O generation predicts large quantities of other spectrally active gases, including HCN (Airapetian et al. 2016, 2020). The production of abiotic HCN and N_2O are strongly linked, because the energetic particles that generate the NH radicals that lead to N_2O production also generate the CH_x radicals that are necessary for HCN production (Airapetian et al. 2016). HCN absorbs most notably at 1.5, 2.5, 3.0, 7.0, and 14 μm, with weaker bands at 1.4, 1.85, and 4.8 μm. The role of HCN in this case would be similar to that proposed for CO and O_4, which can fingerprint abiotic O_2 (Harman et al. 2015; Schwieterman et al. 2016; Meadows et al. 2018b). Similarly, CMEs generate large amounts of potentially detectable HNO_3 at 5.9, 7.5, and 11.3 μm for O_2-rich atmospheres (Tabataba-Vakili et al. 2016). The third panel of Figure 13 provides a conceptual illustration of how we may distinguish the abiotic N_2O due to SPEs from true positive N_2O biosignatures.

We note that predictions of HCN in conjunction with abiotic N_2O are predicated on the presence of the HCN precursor CH_4. According to Airapetian et al. (2016), this CH_4 would directly shield against N_2O photolysis, which would otherwise be a strong sink for N_2O (see Section 3.2). However, while Airapetian et al. (2016) argued that CH_4 provides shielding to wavelengths <230 nm, other sources for CH_4 cross sections indicate a threshold cutoff for strong CH_4 absorption at

$\sim$ > 150 nm (Keller-Rudek et al. 2013). Future work should investigate the impact of differing implementations of CH_4 cross sections on abiotic N_2O production.

The production of N_2O by SPEs generates a potentially identifiable altitude profile of N_2O. Since N_2O is preferentially generated in the stratosphere, concentrations are substantially higher than in the troposphere by a factor of $\sim$1000 (Airapetian et al. 2020). This prediction is a notable deviation from the appearance of N_2O profiles given a surface source (e.g., Figure 9) where concentrations are maximal in the troposphere. If altitude-dependent N_2O (or HCN) profiles can be retrieved, a surface biological source of N_2O could be distinguished from an atmospheric one.

5.3. Is Chemodenitrification a Possible False Positive?

Chemodenitrification can produce abiotic N_2O via reduction of NO_x species by ferrous iron (e.g., $4Fe^{2+} + 2NO_2^- + 5H_2O \rightarrow 4FeOOH + N_2O + 6H^+$; Jones et al. 2015). Chemo-denitrification is observed in one of the very rare metabolically inert environments on Earth, the hypersaline Don Juan Pond in Antarctica (Samarkin et al. 2010; Peters et al. 2014). Chemodenitrification may have played a role in maintaining clement climates on early Earth, when intermediate oxygenation levels may have allowed ferruginous (Fe^{2+}-rich) oceans and oxidized nitrogenous intermediates from denitrification and

nitrification (NO, NO_2^-) to exist together in meaningful concentrations (Stanton et al. 2018). In this scenario, nitrogenous intermediates are biologically generated in an oxic upper ocean layer and subsequently mixed into a deeper Fe^{2+}-rich anoxic layer, where chemodenitrification can take place. Stanton et al. (2018) find that in the end-member chemodenitrification scenario, where all nitrogenous intermediates are released as N_2O via the abiotic oxidation of ferrous iron, parts per million N_2O can be achieved, which is comparable to our maximum N_2O concentrations for the Sun, assuming modern denitrification fluxes. A critical question is whether this scenario is a potential false positive for N_2O biosignatures. The short answer is no, because it relies on the existence of a large pool of nitrogen oxides in the ocean, which is out of equilibrium with a reducing ocean. The pool of nitrogenous intermediates is a product of biological nitrification and denitrification processes. In effect, chemodenitrification in this context short-circuits biological denitrification for the step between NO_2^- and NO or the step between NO and N_2O, with a more efficient abiotic step that produces abiotic N_2O from biotic N substrates. The large flux of N_2O would thus fingerprint (de)nitrification fluxes that are sufficiently large to be attributed to a biosphere, albeit indirectly, and so should not complicate biosignature interpretations.

Another important consideration is whether large pools of abiotic aqueous nitrogen oxides coexist with a ferruginous ocean. We consider this unlikely. The biological nitrification of NH_4^+ to NO_3^- (NH_4^+ $NH_2OH \rightarrow NO \rightarrow NO_2^-$ NO_3^-) requires oxygen. Other sources of NO_x species, such as lightning, are likely to be much weaker, as they have been on Earth since the Archean (Navarro-Gonzalez & Mvondo 2001). In an abiotic O_2 atmosphere, perhaps NO_x species produced by lightning could accumulate over time to saturation in the ocean. However, in this scenario, there would likely be no Fe^{2+} intermediate to reduce these NO_x species to N_2O. Chemodenitrification requires both oxic and anoxic regions within the ocean, which requires substantial fluxes of both oxidants (e.g., O_2) and reductants (e.g., Fe^{2+}). An atmosphere that has accumulated abiotic O_2 would have done so because abiotic O_2 production has completely overwhelmed reductant sinks. Conversely, a flux of reductants sufficiently large to maintain an anoxic ocean layer would be inimical to the maintenance of an abiotic O_2 atmosphere, which would disappear over relatively short geologic timescales. Indeed, past predictions of abiotic O_2 accumulation assumed an ocean saturated in O_2, as otherwise this condition would not occur (Hu et al. 2012, 2020; Domagal-Goldman et al. 2014; Tian et al. 2014; Harman et al. 2018). The presence of N_2O, which lies at an intermediate redox state to O_2 and Fe^{2+}, is an indirect indicator of ocean disequilibrium that excludes abiotic O_2 atmospheres that are stable over geologic time.

Recent laboratory experiments of haze formation under Proterozoic-like N_2–CO_2–CH_4–O_2 atmospheric conditions have suggested the possibility of nitrogen fixation facilitated by the presence of haze particles (Hörst et al. 2018). If this process were very efficient in a Proterozoic-like atmosphere, NO_x species could be delivered to the ocean, which would be subjected to denitrification via biological metabolism or chemodenitrification in an Fe^{2+}-rich ocean, with the possible evolution of N_2O. However, the very presence of the haze requires the simultaneous presence of O_2, CH_4, and N_2, a strong atmospheric and oceanic disequilibrium that correspondingly requires large fluxes of O_2

and CH_4 (Zerkle et al. 2012; Krissansen-Totton et al. 2016, 2018). In this case, the resulting N_2O remains an indirect indicator of this ocean and atmospheric disequilibrium, which is ultimately the result of biology. Furthermore, this N_2O is likely a more observable biosignature than the trace levels of O_2 (2 ppm to 0.2%) that are required to trigger nitrogen fixation in the haze (Hörst et al. 2018).

Another possibility is a large lightning flux on a planet with a slightly reducing atmosphere and ocean and high CO_2 concentrations ($>\sim$100 PAL), such as those hypothesized for the early Archean or late Hadean Earth, along with an intermittently warmer and wetter climate and an increased convection rate (Catling & Zahnle 2020). Wong et al. (2017) proposed that lightning on the early Earth could have generated relevant levels of NO_x species, which could accumulate to prebiotically relevant concentrations in the ocean. However, Ranjan et al. (2019) argued that these NO_x species would be efficiently converted to N_2 or N_2O gas, partially via reaction with Fe^{2+} in the ocean. We also consider it unlikely that these lightning-induced NO_x species would ultimately lead to detectable N_2O in a prebiotic Earthlike atmosphere, because such an atmosphere would lack the O_2 (and O_3) shielding that facilitates large N_2O buildup. The NO_x production rates predicted by Wong et al. (2017) and Ranjan et al. (2019) depend on atmospheric assumptions, such as pCO_2 and pN_2. The largest predicted lightning-induced NO_x flux from Wong et al. (2017) for $pCO_2 = 1$ bar is 6.5×10^8 molecules cm^{-2} s^{-1} ($\sim$0.2 Tmol yr^{-1}). If we assume that 100% of this flux is converted into N_2O, we predict a $\sim$1–100 ppb level of N_2O for all stars, even at an atmospheric pO_2 of 1% PAL (Figures 4 and 5). The calculated N_2O is likely to be even lower with no O_2 and its attendant shielding effects. (Note that we do not consider shielding from 1 bar of CO_2.) NO_2 is a direct product of lightning and is spectrally active at 6.2 μm (Gordon et al. 2022). Future work should quantify the limits of N_2O detectability for lifeless atmospheres and spectral discriminants for false positives in more detail, but at present we consider potential false positives for N_2O as a biosignature to be either implausible or readily diagnosable when viewed in context (Figure 13).

5.4. Potential for Seasonal N_2O Signatures

Seasonal variations in atmospheric gases, including CH_4, CO_2, or O_2/O_3, could potentially be interpreted as a biosignature with the right planetary context (Meadows 2006, 2008; Olson et al. 2018b; Schwieterman 2018). Seasonality can be driven by planetary obliquity, as on Earth today, or by large orbital eccentricity (Gaidos & Williams 2004; Olson et al. 2018b). We do not explicitly explore N_2O seasonality as a potential biosignature here, but our results are relevant for future work on this topic. Seasonal variations in atmospheric biosignature gases will be the result of the interplay between time-dependent production, time-dependent photochemical destruction, and temperature-dependent solubility (Olson et al. 2018b). The photochemical lifetime of N_2O on Earth is around 120 yr (Prather et al. 2015), which is substantially greater than the lifetime of CH_4, which is about 10 yr (Voulgarakis et al. 2013). Correspondingly, the observed relative seasonal variability of N_2O on modern Earth is markedly lower than that of CH_4, about $\sim$0.1%–0.3% for N_2O (Jiang et al. 2007) compared to $\sim$1%–2% for CH_4 (Rasmussen & Khalil 1981; Dlugokencky et al. 2017),

depending on latitude. The seasonal destruction of N_2O is less impacted by temperature than CH_4, because CH_4 is primarily destroyed by OH radicals that are ultimately liberated from tropospheric H_2O (Khalil & Rasmussen 1983). Warmer temperatures lead to more tropospheric H_2O, and thus more OH and less CH_4. In contrast, N_2O is primarily destroyed by photolysis, with a smaller impact from $O(^1D)$ radicals that are sourced from O_3 rather than H_2O.

The greatest seasonal impact will occur when high seasonally variable biological fluxes are matched with high (potentially seasonally variable) photochemical destruction rates (low photochemical lifetimes). Eccentric planets are likely the best targets for seasonal variability, because seasonality driven by eccentricity can avoid many of the degeneracies that are expected on planets with seasonality driven by obliquity. In the case of obliquity, the signal of seasonality can be muted by the mixing of offsetting hemispheric trends, depending on viewing geometry (Olson et al. 2018b). Moreover, the decay and rise of atmospheric gases as a function of the changes in orbital position driven by eccentricity can be more directly linked to inferred global molecular fluxes, which is fundamental to biosignature interpretations.

Based on our results, the highest photochemical destruction rates for N_2O will occur for low-O_2 planets orbiting F- or G-type stars (Figures 4 and 5). Indeed, biologically modulated seasonality in O_2 (and O_3) themselves, as explored by Olson et al. (2018b), would strongly contribute to this relationship. Of course, there is an interplay between the baseline concentration of a gas and its relative variability when considering detectability. We suggest that future studies of N_2O seasonality should explore the phasing and interplay between seasonally dependent denitrification fluxes and seasonal O_2/O_3 concentrations for planets with intermediate oxygenation states orbiting F and G stars, as this set of criteria will maximize the chance of predicting observable N_2O seasonality.

5.5. Study Limitations and Alternative Atmospheric Scenarios

In this study, we have examined N_2O flux–abundance relationships and related photochemistry for Earth-size terrestrial planets with N_2–O_2 dominated atmospheres. We have tested the sensitivity of these flux–abundance relationships to changes in O_2 concentrations, from 1% to 100% PAL for FGKM stellar hosts (Figures 4–9; also see Figure A1). These conditions are motivated in part by the observation that robust biological N_2O production on Earth requires the presence of oxygen to generate the necessary nitrogenous intermediates (e.g., see Figures 1–2), and N_2 is required as a reservoir of N to support the nitrogen cycle. However, we can consider alternative atmospheric scenarios.

The biological production of N_2O on moderately reducing, Archean-like worlds might be facilitated by the presence of oxygen oases that are inhabited by oxygenic photosynthesizers. Oxygen oases have been proposed as possible features of the late Archean Eon on Earth (Anbar et al. 2007; Olson et al. 2013; Reinhard et al. 2013; Riding et al. 2014). However, the flux–abundance relationships of such worlds would fall below those predicted for our 1% PAL O_2 scenarios, illustrated in Section 3.2, due to the lack of shielding effects by O_2 and O_3.

We did not explicitly consider a moist greenhouse state, which may enhance convection and, potentially, lightning rates and NO_x production (Tost et al. 2007; Sergeev et al. 2020). The production of NO_x species, however, will not result in appreciable N_2O buildup via chemodenitrification without the presence of a stratified ocean with both oxygen-rich and anoxic layers, such as existed during the Proterozoic Eon on Earth. As discussed in Section 5.3, a redox stratified ocean is unstable without continuous sources of oxidants and reductants, and N_2O is an intermediate redox product of this likely biologically supported disequilibrium. Nonetheless, future work could explore the rate of NO_x production on worlds with moist greenhouses, including the incorporation of differing circulation regimes on tidally locked planets (Sergeev et al. 2020). An end-member state would be a so-called "steam atmosphere" (e.g., Mousis et al. 2020). A steam atmosphere may be a poor candidate for searching for N_2O biosignatures, however, because the deep atmosphere will contain a supercritical water layer above the surface—with temperature conditions that exclude life as we know it.

Conceivably, some level of N_2O could be generated as a tertiary metabolic product on anoxic planets, potentially including worlds with H_2-dominated atmospheres, as suggested by Seager et al. (2013a, 2013b). The generation of N_2O on a highly reducing world would require the presence of terminal electron acceptors (oxidants), which would likely be scarce in such an environment. However, if the N_2O is nonetheless generated in sufficient abundance, it would be more easily detectable in transit transmission observations, due to the enhanced scale height (Seager et al. 2013a, 2013b). Future work would be needed to fully explore the flux–abundance relationships and, as a consequence, detectability estimates for N_2O in H_2-dominated planetary atmospheres.

Our study used a 1D photochemical model and assumed vertical mixing consistent with an Earth average. Exoplanets, particularly those with different circulation regimes, could have substantially different vertical mixing efficiencies (Zhang & Showman 2018). Enhanced vertical mixing would lead to larger N_2O photolysis rates and less N_2O for any given surface flux. We quantify the impact of adjusting the eddy diffusion profile upward by a factor of 10 on a subset of our flux–abundance calculations in Appendix Figure A4, finding small to modest declines in the predicted surface N_2O mixing ratios. 3D models can more accurately model atmospheric circulation, particularly for tidally locked planets, which may result in hemispheric gradients (Chen et al. 2018, 2019; Yates et al. 2020). Alternative predictions for ozone and other trace gas concentrations would also impact chemistry-climate feedbacks (Gómez-Leal et al. 2019; Yates et al. 2020). We note that Chen et al. (2018) found that the day–night hemisphere contrasts in mixing ratios on synchronously rotating planets differ by only $\sim$20% for standard biosignatures gases like CH_4 and N_2O, so the overall impact of the simplifications inherent in 1D modeling may be small compared to other factors (such as stellar type and bulk atmospheric composition). Nonetheless, future work should more fully explore the impacts of varied circulation regimes on N_2O flux–abundance relationships and potential detectability.

Finally, we further emphasize some of the fundamental assumptions that have been made in this study that will not apply in all scenarios. We have assumed that all modeled planets had N_2 atmospheres with a nitrogen reservoir that would not be limiting for biological nitrification and denitrification. N_2 is an expected volcanic product on terrestrial planets (Schaefer & Fegley 2010), and stellar nitrogen

abundances closely track carbon abundances and overall metallicity in the solar neighborhood (Hinkel et al. 2014). However, the primordial origin of nitrogen during the formation of the planets in the inner solar system, particularly the relative importance of delivery from volatile rich bodies formed outside the ice line, is the subject of ongoing debate (Marty 2012; Alexander et al. 2017; Grewal et al. 2021), and therefore the likelihood and efficiency of this delivery mechanism on exoplanets is unresolved. Planets with substantially lower nitrogen abundances by several orders of magnitude compared to Earth could have biospheres that are limited by the availability of nitrogen. In this case, the capacity of a planetary biosphere to produce any biosignature, including N_2O, would be highly suppressed. On the other hand, N_2-rich planets may have substantially larger atmospheric masses and N_2 partial pressures compared to Earth. We quantify the impact of N_2 partial pressure between 0.5 and 10 bars in Appendix Figure A3, finding negligible declines in the predicted N_2O for the 0.5 bar scenario and modest increases in the predicted N_2O for the 10 bar cases.

Habitable planets in the outer habitable zones of their host stars may be expected to have vastly larger CO_2 abundances, due to the coupling between greenhouse physics and the carbonate-silicate weathering thermostat, possibly as high as 5–20 bars (Kasting et al. 1993; Kopparapu et al. 2013; Rushby et al. 2018; Schwieterman et al. 2019b). We did not model high CO_2 atmospheres, in part because we considered Earthlike planets with Earthlike instellations, which would be inconsistent with these very high CO_2 abundances. We predict that lower instellations would result in less N_2O photolysis, and therefore higher N_2O concentrations, at a given flux. Additionally, CO_2 would provide additional shielding effects at wavelengths shorter than ~200 nm, which could enhance N_2O concentrations, assuming constant O_2 and O_3 shielding. However, the likelihood of oceanic and atmospheric oxygenation on outer habitable-zone planets, and therefore the potential for robust N_2O production and photochemical stability, has yet to be explored. We reserve the studying of these high-CO_2 scenarios for future work.

We modeled Earthlike atmospheres on planets orbiting M-dwarf stars, though the capacity of M-dwarf planets in the continuous habitable zone to retain atmospheres in the face of a long-lived superluminous pre-main-sequence phase and attendant XUV radiation is unresolved (Ramirez & Kaltenegger 2014; Luger & Barnes 2015; Tian 2015). Mass–radius studies of the TRAPPIST-1 system hint that some of these planets retain atmospheres (Grimm et al. 2018; Agol et al. 2021); however, this question will only be definitively resolved by near-future observations by JWST or future telescopes. If M-dwarf planets tend not to retain atmospheres, our results are still valid for the FGK stellar hosts modeled.

5.6. Future Prospects for Detecting N₂O on Exoplanets

The detectability of N_2O spectroscopic biosignatures will also depend on the observing mode (e.g., transit transmission or direct-imaging spectroscopy), the accessible wavelength range, the characteristics of the observed system, and the specifics of the instrument(s) and observing strategy (e.g., Fujii et al. 2018). Because the strongest bands of N_2O lie in the NIR (e.g., 2.9 and 4.5 μm) and MIR (e.g., 7.8 and 8.5 μm), these are more amenable targets for observing techniques that rely on IR transit transmission and/or emission spectroscopy

(Line et al. 2019). Reflected light direct-imaging missions, such as the 6 m IR/O/UV telescope recommended by Astro2020 (National Academies of Sciences, Engineering, and Medicine 2021), will be unlikely to detect N_2O, due to the weak N_2O bands shortward of 2 μm near the expected cutoff for such a mission (The LUVOIR Team 2019; Gaudi et al. 2020). JWST is unlikely to detect N_2O on transiting planets with abundances or fluxes like those of Earth today (e.g., Pidhorodetska et al. 2020; Wunderlich et al. 2021). However, we have shown that N_2O is plausibly detectable on TRAPPIST-1e, assuming an N_2–O_2 atmosphere and a biosphere that emits a large fraction of its total denitrification flux as N_2O. Moreover, intermediate-to-high levels of N_2O could be detected in emitted light by 30 m ground-based telescopes (López-Morales et al. 2019) or by a space-based IR interferometer, such as the LIFE concept mission (Quanz et al. 2022; Alei et al. 2022). Future cooled IR missions may plausibly target the $O_3 + N_2O$ biosignature couple, as investigated by the Origins concept mission report (Meixner et al. 2019). Snellen et al. (2017) propose using a novel high-pass spectral filtering technique to detect the 15 μm CO_2 band on Proxima Centauri b using JWST's MIRI in Medium Resolution Spectrograph mode. Planet/star contrast ratios are particularly favorable at MIR wavelengths. Conceivably, if this technique can successfully reveal atmospheric CO_2, a similar technique could be used to target the 17 μm N_2O band. We suggest that future work quantifying the detectability of biosignature gases should consider the possibility of the elevated N_2O levels that we explore here.

6. Conclusions

We have conducted a systematic study of N_2O flux–abundance relationships for N_2-dominated atmospheres over a large range of surface molecular fluxes (0.01–100 Tmol yr^{-1}), for O_2 abundances ranging from weakly to fully oxygenated (1%–100% PAL), and for potential host stars spanning the entire main sequence, from F4V to M8V. We used the biogeochemical model cGENIE to inform the maximum plausible N_2O fluxes for an Earthlike biosphere, which could be 1–2 orders of magnitude larger than those on present-day Earth, assuming nutrient-rich oceans and evolutionary or environmental conditions that limit the last step in the denitrification process. Even for maximal biospheric N_2O fluxes of 100 Tmol yr^{-1}, an Earthlike atmosphere will never enter an N_2O runaway, but would attain much larger concentrations than those found on Earth today. We find that late K-dwarf and inactive early M-dwarf stars can maintain the highest N_2O levels at any given surface flux, potentially exceeding 1000 ppm. We show that for N_2O fluxes of 10–100 Tmol yr^{-1}, JWST could detect N_2O at 2.9 μm on TRAPPIST-1e within its mission lifetime. In thermal emission spectra, N_2O features at 7.8 and 8.5 μm become comparable to other gaseous features, such as O_3 at ~1 Tmol yr^{-1} for late K dwarfs and 1–10 Tmol yr^{-1} for G dwarfs. Terrestrial planets orbiting K-dwarf stars are particularly appealing targets for N_2O searches with future MIR missions, due to favorable planet–star angular separations and because N_2O fluxes of only 2 to 3 times those of Earth's modern global average can produce N_2O signatures comparable to those of O_3. Only the 8.5 μm band of N_2O is likely to be accessible in thermal emission for M dwarfs, due to the overlap from an enhanced 7.7 μm CH_4 band, but the 8.5 μm feature becomes comparable to O_3 for N_2O fluxes between 1 and 10 Tmol yr^{-1}. Fully abiotic sources of

N$_2$O are limited, and false positives can be identified by relevant astrophysical and planetary context, including complementary spectral signatures.

Appendix A

Figure A1 displays the surface N$_2$O mixing ratios in the same format as Figures 7 and 8, but for an Earthlike planet with pO$_2$ = 10% PAL.

Figure A2 shows the balance between the photolysis (N$_2$O + hν [$\lambda < 240$ nm] $\rightarrow$ N$_2$ + O(^{1}D)) and radical (N$_2$O + (O^{1}D) $\rightarrow$ N$_2$ + O$_2$ and N$_2$O + O(^{1}D) $\rightarrow$ NO + NO) destruction channels as a function of the N$_2$O mixing ratio for four potential stellar hosts (TRAPPIST-1 [M8V], AD Leonis [M3.5Ve], HD 85512 [K6V], and the Sun [G2V]), with pO$_2$ = 100% PAL. Loss rates are calculated for the corresponding scenarios in Figure 6.

Figure A3 shows a sensitivity test where a subset of the simulations from Figure 6 were run with different total surface pressures of 0.5, 1, and 10 bar. The N$_2$ partial pressure was adjusted to attain these different total pressures, while the total O$_2$ partial pressures were fixed at 100% PAL (i.e., 0.21 bars), to isolate the effects of pressure structure from the total O$_2$ column densities. The subset of stellar spectra chosen spans most of the main sequence and encompasses the minima and maxima of the observed flux–abundance relationships. To facilitate direct intercomparison, the N$_2$O mixing ratios were adjusted to reflect the effective mixing ratio if the total pressure were 1 bar (e.g., the 10 bar surface mixing ratios were multiplied by 10). Simulations with a total pressure of 0.5 bar show very slight reductions in N$_2$O at a given flux compared to the corresponding 1 bar case. Simulations with total pressures of 10 bar show enhanced N$_2$O abundances at a given flux, by a larger factor of up to ~2–3, most notably for the Earth–Sun cases. The N$_2$O abundance enhancements at high pressure were due to the adjustment of the
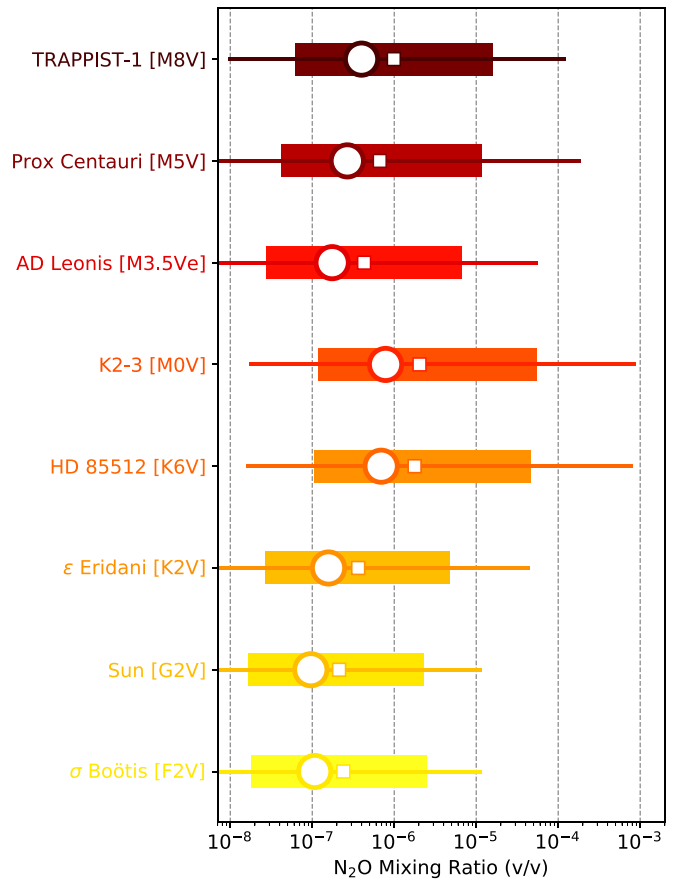

Figure A1. The same as Figures 7 and 8, but for an Earthlike planet with pO$_2$ = 10% PAL.

altitudes where O(^{1}D) was formed. In the 10 bar cases, O(^{1}D), the secondary sink for N$_2$O, was most effectively formed in the upper atmosphere, where N$_2$O concentrations were lower due to photolysis, reducing the impact of this photochemical sink. Correspondingly, the largest pressure effect is seen in the Sun cases, where O(^{1}D) is a proportionally larger sink than it is for other stellar types (see Figure A2). This sensitivity test demonstrates that high-pressure atmospheres will facilitate enhanced N$_2$O abundances at fixed O$_2$ partial pressures and fixed N$_2$O fluxes. Importantly, the general slopes of the flux–abundance relationships for each star are robust to differences in the partial pressures of inert gases.

Figure A4 shows a sensitivity test where a subset of the simulations from Figure 6 were run with an eddy diffusion (k_{zz}) profile increased by a factor of 10 from the default Earth values above the troposphere. (This results in a shift from an average of ~10^4–~10^5 cm^{-2} s^{-1} at 30 km). The cases with an increased eddy diffusion profile have lower concentrations by a maximum of a factor of ~3, due to more effective transport to the upper atmosphere, where N$_2$O can be more easily photolyzed. The sensitivity of the N$_2$O concentrations to the assumed k_{zz} profile is substantially reduced for the later stellar types (K6V and M5V) versus the Sun, due to the difference in the spectral distribution of stellar UV photons between the stars and the increased importance of N$_2$O self-shielding at higher N$_2$O concentrations. The slopes of the flux–abundance relationships for each star are robust to uniform increases in assumed k_{zz}.
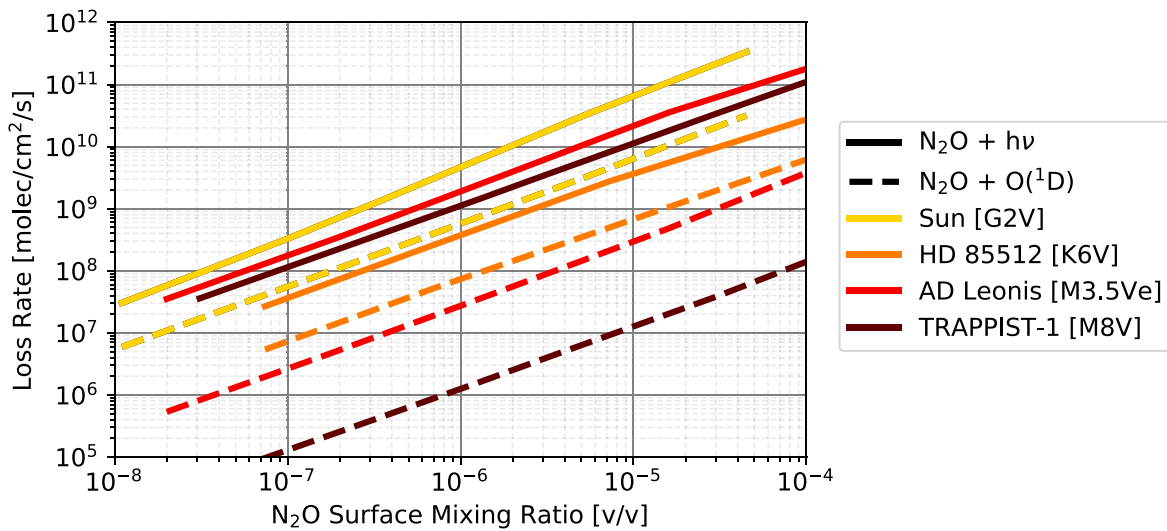
Figure A2. Photochemical reaction rates for the two major N_2O destruction pathways as a function of stellar type. The solid lines represent the N_2O photolysis rates, while the dotted lines represent the destruction of N_2O by singlet oxygen $O(^1D)$. The calculations assume $pO_2 = 100\%$ PAL.
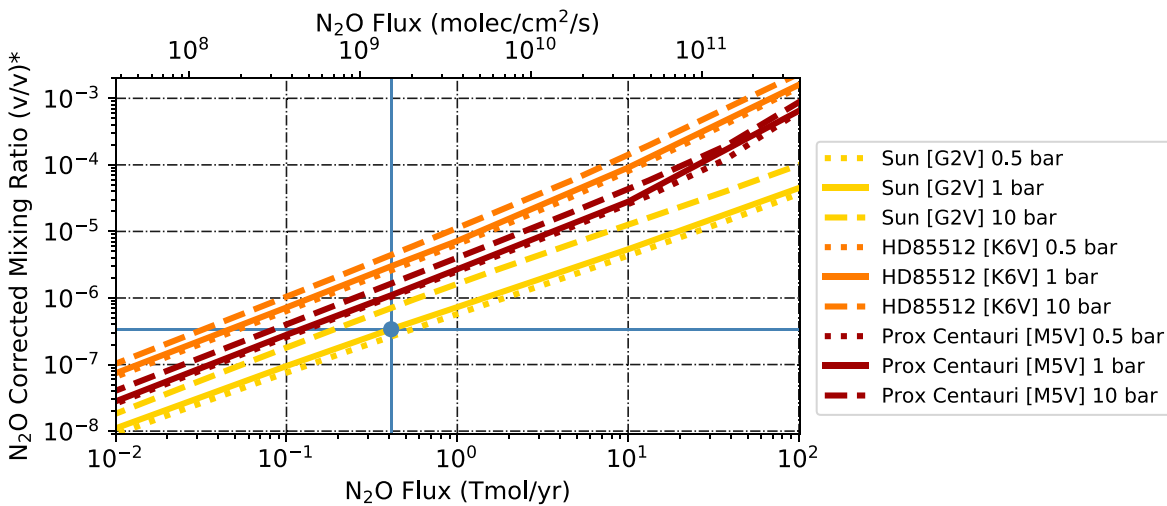

Figure A3. Sensitivity test showing the atmospheric mixing ratios of N_2O as a function of surface flux for an Earthlike atmosphere with $pO_2 = 100\%$ PAL and total pressures of 0.5 bar (dotted lines), 1 bar (solid lines), and 10 bar (dashed lines). The total pressures are adjusted by changing the N_2 partial pressures, while the O_2 partial pressure is fixed at 0.21 bar. N_2O mixing ratios are recalculated to reflect the effective mixing ratio if the total pressure were 1 bar.
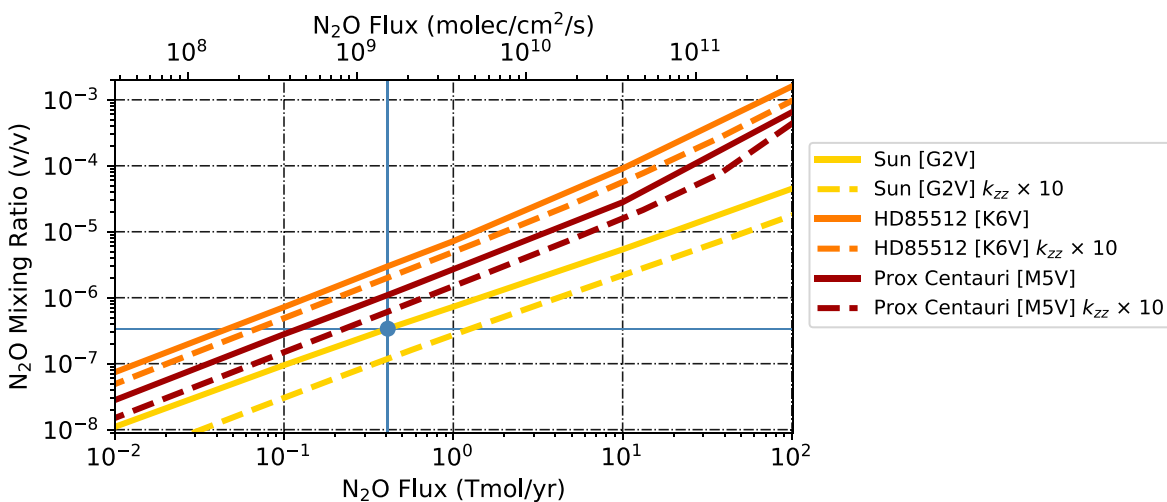

Figure A4. Sensitivity test showing the atmospheric mixing ratios of N_2O as a function of surface flux for an Earthlike atmosphere with $pO_2 = 100\%$ PAL and an eddy diffusion (k_{zz}) profile matching the Earth average (solid) and increased by a factor of 10 uniformly through the upper atmosphere (dashed).

ORCID iDs

Edward W. Schwieterman ● https://orcid.org/0000-0002-2949-2163
Stephanie L. Olson ● https://orcid.org/0000-0002-3249-6739
Daria Pidhorodetska ● https://orcid.org/0000-0001-9771-7953
Thomas J. Fauchez ● https://orcid.org/0000-0002-5967-9631
Sandra T. Bastelberger ● https://orcid.org/0000-0003-2052-3442
Jaime S. Crouse ● https://orcid.org/0000-0003-2273-8324
Andy Ridgwell ● https://orcid.org/0000-0003-2333-0128

References

Agol, E., Dorn, C., Grimm, S. L., et al. 2021, PSJ, 2, 1
Airapetian, V. S., Barnes, R., Cohen, O., et al. 2020, IJAsB, 19, 136
Airapetian, V. S., Danchi, W. C., Dong, C. F., et al. 2018, arXiv:1801.07333
Airapetian, V. S., Glocer, A., Gronoff, G., et al. 2016, NatGe, 9, 452
Alei, E., Konrad, B. S., Angerhausen, D., et al. 2022, arXiv:2204.10041
Alexander, C. M. O. D., Cody, G. D., De Gregorio, B. T., et al. 2017, ChEG, 77, 227
Anbar, A. D., Duan, Y., Lyons, T. W., et al. 2007, Sci, 317, 1903
Anbar, A. D., & Knoll, A. H. 2002, Sci, 297, 1137
Anglada-Escudé, G., Amado, P. J., Barnes, J., et al. 2016, Natur, 536, 437
Arney, G., Domagal-Goldman, S. D., Meadows, V. S., et al. 2016, AsBio, 16, 873
Arney, G. N. 2019, ApJL, 873, L7
Barnett, M. N., & Olson, S. L. 2022, PSJ, 3, 132
Buick, R. 2007, Geobiology, 5, 97
Canfield, D. E., Glazer, A. N., & Falkowski, P. G. 2010, Sci, 330, 192
Cao, L., Eby, M., Ridgwell, A., et al. 2009, BGeo, 6, 375
Carreira, C., Pauleta, S. R., & Moura, I. 2017, J. Inorg. Biochem., 177, 423
Catling, D. C., Krissansen-Totton, J., Kiang, N. Y., et al. 2018, AsBio, 18, 709
Catling, D. C., & Zahnle, K. J. 2020, SciA, 6, eaax1420
Checlair, J. H., Villanueva, G. L., Hayworth, B. P. C., et al. 2021, AJ, 161, 150
Chen, H., Mothapo, N. V., & Shi, W. 2015, MicEc, 69, 180
Chen, H., Wolf, E. T., Kopparapu, R., et al. 2018, ApJL, 868, L6
Chen, H., Wolf, E. T., Zhan, Z., et al. 2019, ApJ, 886, 16
Christianson, J. L. 2022, NatAs, 6, 516
Crutzen, P. J., Isaksen, I. S. A., & Reid, G. C. 1975, Sci, 189, 457
Defrère, D., Léger, A., Absil, O., et al. 2018, ExA, 46, 543
Delgado Mena, E., Tsantaki, M., Adibekyan, V. Z., et al. 2017, A&A, 606, A94
Des Marais, D. J., Harwit, M. O., Jucks, K. W., et al. 2002, AsBio, 2, 153
Dlugokencky, E. J., Crotwell, A. M., Lang, P. M., et al. 2017, Version 2017-01-20, ftp://cmdl.noaa.gov/data/trace_gases/ch
Domagal-Goldman, S. D., Segura, A., Claire, M. W., et al. 2014, ApJ, 792, 43
Ducrot, E., Gillon, M., Delrez, L., et al. 2020, A&A, 640, A112
Falkowski, P., Scholes, R. J., Boyle, E., et al. 2000, Sci, 290, 291
Faria, J. P., Suárez Mascareño, A., Figueira, P., et al. 2022, A&A, 658, A115
Fauchez, T. J., Turbet, M., Villanueva, G. L., et al. 2019, ApJ, 887, 194
Fauchez, T. J. T. J., Villanueva, G. L. G. L., Schwieterman, E. W., et al. 2020, NatAs, 4, 372
Fennel, K., Follows, M., & Falkowski, P. G. 2005, AmJS, 305, 526
France, K., Loyd, R. O. P., Youngblood, A., et al. 2016, ApJ, 820, 89
Fujii, Y., Angerhausen, D., Deitrick, R., et al. 2018, AsBio, 18, 739
Gaidos, E., & Williams, D. M. 2004, NewA, 10, 67
Gaudi, B. S., Seager, S., Mennesson, B., et al. 2020, arXiv:2001.06683
Gillon, M., Triaud, A. H. M. J., Demory, B.-O., et al. 2017, Natur, 542, 456
Gómez-Leal, I., Kaltenegger, L., Lucarini, V., et al. 2019, Icar, 321, 608
Gordon, I. E., Rothman, L. S., Hargreaves, R. J., et al. 2022, JQSRT, 277, 107949
Grenfell, J. L., Gebauer, S., Godolt, M., et al. 2013, AsBio, 13, 415
Grenfell, J. L., Gebauer, S. V, Paris, P., et al. 2014, P&SS, 98, 66
Grenfell, J. L. 2017, PhR, 713, 1
Grewal, D. S., Dasgupta, R., & Marty, B. 2021, NatAs, 5, 356
Grimm, S. L., Demory, B.-O., Gillon, M., et al. 2018, A&A, 613, A68
Gruber, N., & Galloway, J. N. 2008, Natur, 451, 293
Haqq-Misra, J., Fauchez, T. J., Schwieterman, E. W., et al. 2022, ApJL, 929, L28
Harman, C. E., Schwieterman, E. W., Schottelkotte, J. C., et al. 2015, ApJ, 812, 137
Harman, C. E., Felton, R., Hu, R., et al. 2018, ApJ, 866, 56

Harris, C. R., Millman, K. J., van der Walt, S. J., et al. 2020, Natur, 585, 357
Hinkel, N. R., Timmes, F. X., Young, P. A., et al. 2014, AJ, 148, 54
Hitchcock, D. R., & Lovelock, J. E. 1967, Icar, 7, 149
Hörst, S. M., He, C., Ugelow, M. S., et al. 2018, ApJ, 858, 119
Hu, J., Airapetian, V. S., Li, G., et al. 2022, SciA, 8, eabi9743
Hu, R., Peterson, L., & Wolf, E. T. 2020, ApJ, 888, 122
Hu, R., Seager, S., & Bains, W. 2012, ApJ, 761, 166
Hunter, J. D. 2007, CSE, 9, 90
Jiang, X., Ku, W. L., Shia, R.-L., et al. 2007, GBioC, 21, 1
Jones, L. C., Peters, B., Lezama Pacheco, J. S., et al. 2015, EnST, 49, 3444
Kaltenegger, L., Pepper, J., Stassun, K., et al. 2019, ApJL, 874, L8
Kaltenegger, L. 2017, ARA&A, 55, 433
Kaltenegger, L., Lin, Z., & Madden, J. 2020a, ApJL, 892, L17
Kaltenegger, L., MacDonald, R. J., Kozakis, T., et al. 2020b, ApJL, 901, L1
Kaltenegger, L., Traub, W. A., & Jucks, K. W. 2007, ApJ, 658, 598
Kane, S. R., Hill, M. L., Kasting, J. F., et al. 2016, ApJ, 830, 1
Kasting, J. F., Liu, S. C., & Donahue, T. M. 1979, JGR, 84, 3097
Kasting, J. F., Whitmire, D. P., & Reynolds, R. T. 1993, Icar, 101, 108
Kawashima, Y., & Rugheimer, S. 2019, AJ, 157, 213
Keller-Rudek, H., Moortgat, G. K., Sander, R., et al. 2013, ESSD, 5, 365
Khalil, M. A. K., & Rasmussen, R. A. 1983, JGR, 88, 5131
Kirtland Turner, S., & Ridgwell, A. 2016, E&PSL, 435, 1
Kopparapu, R. K., Ramirez, R., Kasting, J. F., et al. 2013, ApJ, 765, 131
Koutný, M., & Kučera, I. 1999, Biochem. Biophys. Res. Commun., 262, 562
Krissansen-Totton, J., Bergsman, D. S., & Catling, D. C. 2016, AsBio, 16, 39
Krissansen-Totton, J., & Catling, D. C. 2020, E&PSL, 537, 116181
Krissansen-Totton, J., Olson, S., & Catling, D. C. 2018, SciA, 4, eaao5747
Krissansen-Totton, J., Thompson, M., Galloway, M. L., et al. 2022, NatAs, 6, 189
Kristjansson, J. K., & Hollocher, T. C. 1980, J. Biol. Chem., 255, 704
Lafferty, W. J., Solodov, A. M., Weber, A., et al. 1996, ApOpt, 35, 5911
Lammer, H., Sproß, L., Grenfell, J. L., et al. 2019, AsBio, 19, 927
Lenton, T. M., Daines, S. J., & Mills, B. J. W. 2018, ESRv, 178, 1
Lewis, N., Clampin, M., Mountain, M., et al. 2017, JWST Proposal Cycle 1, 1331, https://www.stsci.edu/jwst/phase2-public/1331.pdf
Lin, Z., MacDonald, R. J., Kaltenegger, L., et al. 2021, MNRAS, 505, 3562
Lincowski, A. P., Meadows, V. S., Crisp, D., et al. 2018, ApJ, 867, 76
Line, M. R., Quanz, S. P., Schwieterman, E. W., et al. 2019, BAAS, 51, 271
López-Morales, M., Currie, T., Teske, J., et al. 2019, BAAS, 51, 162
Lovelock, J. E. 1965, Natur, 207, 568
Lovelock, J. E. 1975, RSPSB, 189, 167
Luger, R., & Barnes, R. 2015, AsBio, 15, 119
Luger, R., Sestovic, M., Kruse, E., et al. 2017, NatAs, 1, 0129
Lustig-Yaeger, J., Meadows, V. S., & Lincowski, A. P. 2019, AJ, 158, 27
Lyons, T. W., & Severmann, S. 2006, GeCoA, 70, 5698
Mahan, B., Siebert, J., Blanchard, I., et al. 2018, JGRB, 123, 8349
Manabe, S., & Wetherald, R. T. 1967, JAtS, 24, 241
Marty, B. 2012, E&PSL, 314, 56
Meadows, V. S. 2006, in Proc. IAU Colloq. 200, Direct Imaging of Exoplanets: Science & Techniques, ed. C. Aime & F. Vakili (Cambridge: Cambridge Univ. Press), 25
Meadows, V. S. 2008, Exoplanets (Chichester: Springer Praxis), 259
Meadows, V. S., Arney, G. N., Schwieterman, E. W., et al. 2018a, AsBio, 18, 133
Meadows, V. S., Reinhard, C. T., Arney, G. N., et al. 2018b, AsBio, 18, 630
Meixner, M., Cooray, A., Leisawitz, D., et al. 2019, arXiv:1912.06213
Morley, C. V., Kreidberg, L., Rustamkulov, Z., et al. 2017, ApJ, 850, 121
Mousis, O., Deleuil, M., Aguichine, A., et al. 2020, ApJL, 896, L22
Naafs, B. D. A., Monteiro, F. M., Pearson, A., et al. 2019, PNAS, 116, 24979
National Academies of Sciences, Engineering, and Medicine 2021, Pathways to Discovery in Astronomy and Astrophysics for the 2020s (Washington, DC: The National Academies Press)
Navarro-Gonzalez, R., & Mvondo, D. N. 2001, Natur, 412, 61
Olson, S., Kump, L. R., & Kasting, J. F. 2013, ChGeo, 362, 35
Olson, S. L., Reinhard, C. T., & Lyons, T. W. 2016, PNAS, 113, 11447
Olson, S. L., Schwieterman, E. W., Reinhard, C. T., et al. 2018a, in Handbook of Exoplanets, ed. H. Deeg & J. Belmont (Cham: Springer), 189
Olson, S. L., Schwieterman, E. W., Reinhard, C. T., et al. 2018b, ApJL, 858, L14
Paraskevopoulos, K., Antonyuk, S. V., Sawers, R. G., et al. 2006, J. Mol. Biol., 362, 55
Parke Loyd, R. O., Shkolnik, E. L., Schneider, A. C., et al. 2018, ApJ, 867, 70
Pauleta, S. R., Dell'Acqua, S., & Moura, I. 2013, Coord. Chem. Rev., 257, 332
Pavlov, A. A., Brown, L. L., & Kasting, J. F. 2001, JGR, 106, 23267
Peacock, S., Barman, T., Shkolnik, E. L., et al. 2020, ApJ, 895, 5
Peacock, S., Barman, T., Shkolnik, E. L., et al. 2019a, ApJ, 886, 77
Peacock, S., Barman, T. S., Schneider, A. C., et al. 2022, ApJ, 933, 235

Peacock, S., Barman, T., Shkolnik, E. L., et al. 2019b, ApJ, 871, 235
Peters, B., Casciotti, K. L., Samarkin, V. A., et al. 2014, GeCoA, 135, 87
Phillips, C. L., Wang, J., Kendrew, S., et al. 2021, ApJ, 923, 144
Pidhorodetska, D., Fauchez, T. J., Villanueva, G. L., et al. 2020, ApJL, 898, L33
Pidhorodetska, D., Moran, S. E., Schwieterman, E. W., et al. 2021, AJ, 162, 169
Planavsky, N. J., Rouxel, O. J., Bekker, A., et al. 2010, Natur, 467, 1088
Prather, M. J., Hsu, J., Deluca, N. M., et al. 2015, JGRD, 120, 5693
Prosser, J. I., & Nicol, G. W. 2012, Trends Microbiol., 20, 523
Quanz, S. P., Absil, O., Angerhausen, D., et al. 2019, arXiv:1908.01316
Quanz, S. P., Kammerer, J., Defrère, D., et al. 2018, Proc. SPIE, 10707, 1070111I
Quanz, S. P., Ottiger, M., Fontanet, E., et al. 2022, A&A, 664, A21
Ramirez, R. M., & Kaltenegger, L. 2014, ApJL, 797, L25
Ranjan, S., Schwieterman, E. W., Harman, C., et al. 2020, ApJ, 896, 148
Ranjan, S., Seager, S., Zhan, Z., et al. 2022, ApJ, 930, 131
Ranjan, S., Todd, Z. R., Rimmer, P. B., et al. 2019, GGG, 20, 2021
Rasmussen, R. A., & Khalil, M. A. K. 1981, JGR, 86, 9826
Rauer, H., Gebauer, S., Paris, P. V., et al. 2011, A&A, 529, A8
Ravishankara, A. R., Daniel, J. S., & Portmann, R. W. 2009, Sci, 326, 123
Reid, I. N., Turner, E. L., Turnbull, M. C., et al. 2007, ApJ, 665, 767
Reinhard, C. T., Lalonde, S. V., & Lyons, T. W. 2013, ChGeo, 362, 44
Reinhard, C. T., Olson, S. L., Kirtland Turner, S., et al. 2020, GMD, 13, 5687
Reinhard, C. T., Olson, S. L., Schwieterman, E. W., et al. 2017a, AsBio, 17, 287
Reinhard, C. T., & Planavsky, N. J. 2022, ARMS, 14, 331
Reinhard, C. T., Planavsky, N. J., Gill, B. C., et al. 2017b, Natur, 541, 386
Reinhard, C. T., Planavsky, N. J., Olson, S. L., et al. 2016, PNAS, 113, 8933
Ribas, I., Bolmont, E., Selsis, F., et al. 2016, A&A, 596, A111
Ridgwell, A., Hargreaves, J. C., Edwards, N. R., et al. 2007, BGeo, 4, 87
Riding, R., Fralick, P., & Liang, L. 2014, PreR, 251, 232
Roberson, A. L., Roadt, J., Halevy, I., et al. 2011, Geobiology, 9, 313
Robinson, T. D., & Reinhard, C. T. 2018, Planetary Astrobiology (Tucson, AZ: Univ. Arizona Press), 10.2458/azu_uapress_9780816540068-ch015
Rugheimer, S., Kaltenegger, L., Segura, A., et al. 2015a, ApJ, 809, 57
Rugheimer, S., Segura, A., Kaltenegger, L., et al. 2015b, ApJ, 806, 137
Rugheimer, S., & Kaltenegger, L. 2018, ApJ, 854, 19
Rugheimer, S., Kaltenegger, L., Zsom, A., et al. 2013, AsBio, 13, 251
Rushby, A. J., Johnson, M., Mills, B. J. W., et al. 2018, AsBio, 18, 469
Sagan, C., Thompson, W. R., Carlson, R., et al. 1993, Natur, 365, 715
Samarkin, V. a., Madigan, M. T., Bowles, M. W., et al. 2010, NatGe, 3, 341
Santoro, A. E., Buchwald, C., McIlvin, M. R., et al. 2011, Sci, 333, 1282
Schaefer, L., & Fegley, B. 2010, Icar, 208, 438
Schumann, U., & Huntrieser, H. 2007, ACPD, 7, 2623
Schwieterman, E. W. 2018, in Handbook of Exoplanets, ed. H. Deeg & J. Belmont (Cham: Springer), 69
Schwieterman, E. W., Kiang, N. Y., Parenteau, M. N., et al. 2018, AsBio, 18, 663
Schwieterman, E. W., Meadows, V. S., Domagal-Goldman, S. D., et al. 2016, ApJL, 819, L13
Schwieterman, E. W., Reinhard, C. T., Olson, S. L., et al. 2019a, ApJ, 874, 9
Schwieterman, E. W., Reinhard, C. T., Olson, S. L., et al. 2019b, ApJ, 878, 19
Schwieterman, E. W., Robinson, T. D., Meadows, V. S., et al. 2015, ApJ, 810, 57
Seager, S., Bains, W., & Hu, R. 2013a, ApJ, 777, 95
Seager, S., Bains, W., & Hu, R. 2013b, ApJ, 775, 104
Seager, S., Schrenk, M., & Bains, W. 2012, AsBio, 12, 61
Segura, A., Krelove, K., Kasting, J. F., et al. 2003, AsBio, 3, 689
Segura, A. A., Kasting, J. F., Meadows, V., et al. 2005, AsBio, 5, 706
Sergeev, D. E., Lambert, F. H., Mayne, N. J., et al. 2020, ApJ, 894, 84
Shkolnik, E. L., & Barman, T. S. 2014, AJ, 148, 64
Snellen, I. A. G., Désert, J.-M., Waters, L. B. F. M., et al. 2017, AJ, 154, 77
Sousa-Silva, C., Seager, S., Ranjan, S., et al. 2020, AsBio, 20, 235
Sproß, L., Scherf, M., Shematovich, V. I., et al. 2021, ARep, 65, 275
Stanton, C. L., Reinhard, C. T., Kasting, J. F., et al. 2018, Geobiology, 16, 597
Stüeken, E. E., Kipp, M. A., Koehler, M. C., et al. 2016, AsBio, 16, 949
Suissa, G., Mandell, A. M., Wolf, E. T., et al. 2020, ApJ, 891, 58
Tabataba-Vakili, F., Grenfell, J. L., Grießmeier, J.-M., et al. 2016, A&A, 585, A96
Teal, D. J., Kempton, E. M.-R., Bastelberger, S., et al. 2022, ApJ, 927, 90
Thamdrup, B. 2012, Annu. Rev. Ecol. Evol. Syst., 43, 407
The LUVOIR Team 2019, arXiv:1912.06219
Thuillier, G., Floyd, L., Woods, T. N., et al. 2004, AdSpR, 34, 256
Tian, F. 2015, E&PSL, 432, 126
Tian, F., France, K., Linsky, J. L., et al. 2014, E&PSL, 385, 22
Tian, H., Chen, G., Lu, C., et al. 2015, Ecosyst. Health Sustain., 1, 1
Tian, H., Xu, R., Canadell, J. G., et al. 2020, Natur, 586, 248
Toon, O. B., Mckay, C. P., Ackerman, T. P., et al. 1989, JGR, 94, 16287
Tost, H., Jöckel, P., & Lelieveld, J. 2007, ACP, 7, 4553
Turnbull, M. C., & Tarter, J. C. 2003, ApJS, 145, 181
Turnbull, M. C. 2015, arXiv:1510.01731
Villanueva, G. L., Liuzzi, G., Faggi, S., et al. 2022, Fundamentals of the Planetary Spectrum Generator (Greenbelt, MD: NASA Goddard Space Flight Center)
Villanueva, G. L., Smith, M. D., Protopapa, S., et al. 2018, JQSRT, 217, 86
Voulgarakis, A., Naik, V., Lamarque, J. F., et al. 2013, ACP, 13, 2563
Wogan, N. F., & Catling, D. C. 2020, ApJ, 892, 127
Wong, M. L., Charnay, B. D., Gao, P., et al. 2017, AsBio, 17, 975
Wunderlich, F., Godolt, M., Grenfell, J. L., et al. 2019, A&A, 624, A49
Wunderlich, F., Scheucher, M., Godolt, M., et al. 2020, ApJ, 901, 126
Wunderlich, F., Scheucher, M., Grenfell, J. L., et al. 2021, A&A, 647, A48
Yates, J. S., Palmer, P. I., Manners, J., et al. 2020, MNRAS, 492, 1691
Youngblood, A., France, K., Loyd, R. O. P., et al. 2016, ApJ, 824, 101
Zahnle, K., Claire, M., & Catling, D. 2006, Geobiology, 4, 271
Zerkle, A. L., Claire, M. W., Domagal-Goldman, S. D., et al. 2012, NatGe, 5, 359
Zhang, X., & Showman, A. P. 2018, ApJ, 866, 1